



# On the viability of determining galaxy properties from observations I: Star formation rates and kinematics

Kearn Grisdale, Laurence Hogan, Dimitra Rigopoulou, Niranjana Thatte, Miguel Pereira-Santaella, Julien Devriendt, Adrienne Slyz, Ismael García-Bernete, Yohan Dubois, Sukyoung K. Yi, et al.

## ► To cite this version:

Kearn Grisdale, Laurence Hogan, Dimitra Rigopoulou, Niranjana Thatte, Miguel Pereira-Santaella, et al.. On the viability of determining galaxy properties from observations I: Star formation rates and kinematics. Monthly Notices of the Royal Astronomical Society, 2022, 10.1093/mnras/stac1124 . insu-03667428

**HAL Id: insu-03667428**

**<https://insu.hal.science/insu-03667428>**

Submitted on 7 Apr 2023

**HAL** is a multi-disciplinary open access archive for the deposit and dissemination of scientific research documents, whether they are published or not. The documents may come from teaching and research institutions in France or abroad, or from public or private research centers.

L'archive ouverte pluridisciplinaire **HAL**, est destinée au dépôt et à la diffusion de documents scientifiques de niveau recherche, publiés ou non, émanant des établissements d'enseignement et de recherche français ou étrangers, des laboratoires publics ou privés.

# On the viability of determining galaxy properties from observations – I. Star formation rates and kinematics

Kearn Grisdale<sup>1</sup>,<sup>1</sup>★ Laurence Hogan,<sup>1</sup> Dimitra Rigopoulou,<sup>1</sup> Niranjana Thatte,<sup>1</sup>  
Miguel Pereira-Santaella,<sup>1,2</sup> Julien Devriendt,<sup>1</sup> Adrienne Slyz,<sup>1</sup> Ismael García-Bernete,<sup>1</sup> Yohan Dubois,<sup>3</sup>  
Sukyoung K. Yi<sup>4</sup> and Katarina Kraljic<sup>5</sup>

<sup>1</sup>Sub-department of Astrophysics, University of Oxford, Keble Road, Oxford OX1 3RH, UK

<sup>2</sup>Centro de Astrobiología (CSIC-INTA), Ctra. de Ajalvir, Km 4, Torrejón de Ardoz, Madrid E-28850, Spain

<sup>3</sup>Institut d'Astrophysique de Paris, UMR 7095, CNRS, UPMC Univ. Paris VI, 98 bis boulevard Arago, F-75014 Paris, France

<sup>4</sup>Department of Astronomy, Yonsei University, 50 Yonsei-ro, Seodaemun-gu, Seoul 03722, Republic of Korea

<sup>5</sup>Aix Marseille Univ, CNRS, CNES, LAM, Marseille, France

Accepted 2022 April 20. Received 2022 April 14; in original form 2022 February 18

## ABSTRACT

We explore how observations relate to the physical properties of the emitting galaxies by post-processing a pair of merging  $z \sim 2$  galaxies from the cosmological, hydrodynamical simulation NEWHORIZON, using LCARS (Light from Cloudy Added to RAMSES) to encode the physical properties of the simulated galaxy into H  $\alpha$  emission line. By carrying out mock observations and analysis on these data cubes, we ascertain which physical properties of the galaxy will be recoverable with the HARMONI spectrograph on the European Extremely Large Telescope (ELT). We are able to estimate the galaxy's star formation rate and dynamical mass to a reasonable degree of accuracy, with values within a factor of 1.81 and 1.38 of the true value. The kinematic structure of the galaxy is also recovered in mock observations. Furthermore, we are able to recover radial profiles of the velocity dispersion and are therefore able to calculate how the dynamical ratio varies as a function of distance from the galaxy centre. Finally, we show that when calculated on galaxy scales the dynamical ratio does not always provide a reliable measure of a galaxy's stability against gravity or act as an indicator of a minor merger.

**Key words:** galaxies: high-redshift – galaxies: kinematics and dynamics – galaxies: structure – cosmology: observations.

## 1 INTRODUCTION

Observations are the primary means by which humanity explores the Universe. Over the next several years new facilities such as the (European) Extremely Large Telescope (ELT), with its 39 m diameter primary mirror, will become operational and present new observational opportunities. Such telescopes will allow higher resolution and deeper observations than current facilities (Tamai et al. 2016; Cirasuolo et al. 2020). This will be pivotal for the study of galaxy formation and evolution, particularly at high redshifts ( $z \gtrsim 1.5$ ). It is therefore vitally important to understand how these observations translate back into the intrinsic properties of galaxies, giant molecular clouds (GMCs), the interstellar medium (ISM), and star formation.

Through multiwavelength observation researchers have been able to determine the star formation rate (SFR) of high redshift galaxies. Such observations have resulted in the measurement of a correlation between SFR and stellar mass ( $M_*$ ) of a galaxy which has since become known as the Main Sequence (MS) of star-forming galaxies (e.g. Daddi et al. 2007; Noeske et al. 2007). Star-forming galaxies can be placed into one of two populations: normal star forming or starbursts. Normal star-forming galaxies lie within the scatter of the MS correlation ( $\sim 0.3$  dex), whereas starbursts are defined as

having a SFR at least four times greater than expected from the MS correlation (Elbaz et al. 2011; Schreiber et al. 2015). Furthermore, it has also been determined that the cosmic star formation rate density (SFRD) evolves with  $z$ , having peaked at  $z \sim 1.9$ , before declining by an order of magnitude to the current epoch (Madau & Dickinson 2014). The normalization of the MS correlation increases with redshift (Speagle et al. 2014) in line with the increase in the cosmic SFRD, which means galaxies at high- $z$  have higher SFRs than those at the current epoch but are not be considered starburst galaxies. For example, at  $z \sim 2$  galaxies on the MS tend to have a SFR of  $\sim 20 \times$  that of an MS galaxy at  $z = 0$ .

A relationship between the gas surface density ( $\Sigma_g$ ) and SFR surface density ( $\dot{\Sigma}_*$ ) of galaxies has also been found, often taking the form of a so-called Kennicutt–Schmidt law:  $\dot{\Sigma}_* \propto \Sigma_g^n$ , with  $n \sim 1.5$  (Schmidt 1959; Kennicutt 1998). The scalings of SFR with  $z$  and  $\Sigma_g$  support observations showing that galaxies at high  $z$  have more gas than galaxies in the local Universe.

Measuring the kinematics of a galaxy can provide key insights into the processes guiding its evolution, such as the source of dynamical support (Puech et al. 2007; Epinat et al. 2009) or determining if a galaxy is undergoing a merger. For example, both the  $K$ -band Multi Object Spectrograph (KMOS) Redshift One Spectroscopic Survey (KROSS) and KMOS<sup>3D</sup> surveys (see Stott et al. 2016; Wisnioski et al. 2019, respectively, and references within) used Integral Field Spectroscopy (IFS) observations of H  $\alpha$  emissions line to calculate

★ E-mail: [kearn.grisdale@physics.ox.ac.uk](mailto:kearn.grisdale@physics.ox.ac.uk)

rotational velocities and velocity dispersions for a number of galaxies at  $0.6 < z < 2.7$ . These studies were able to determine whether or not a given galaxy in their sample was rotationally dominated. Such determinations can be made by comparing the rotational velocity to the velocity dispersion (commonly known as  $v_\theta/\sigma$  and first introduced by Binney 1978). Alternatively, it is possible to use stability criteria such as the classic Toomre ‘ $Q$ ’ (Toomre 1964) or the more recent Romeo dispersion relation (Romeo, Burkert & Agertz 2010).

Recently, Hogan et al. (2021), hence forth H21, performed observations, using the KMOS on the Very Large Telescope (VLT), of a sample of luminous Infra-Red (IR) galaxies, at  $2 < z < 2.5$ . The goal of this work was to establish whether  $z \sim 2$  luminous IR galaxies are isolated or interacting discs. H21 established that a significant fraction,  $\sim 40$  per cent, appear to be isolated galaxies based on their properties, such as  $v_\theta/\sigma$ , their position on the MS, and their levels of dust obscured star formation when compared to local starburst galaxies. H21 determined that the huge SFR seen in IR luminous galaxies at cosmic noon can be powered by steady-state mechanisms and do not require stochastic events, such as the gas rich major mergers that power local ultraluminous infrared galaxies.

All of these observations require some method for converting the photons received from a galaxy into physical measurements of its properties, e.g. multiplying the integral of an emission line by a conversion factor to get an SFR (see Kennicutt, Tamblyn & Congdon 1994). Cosmological simulations can provide useful insight into observations by running their suites, each with different physical models, and comparing the results to observations. For example, Grisdale et al. (2017) compared the power spectrum calculated from H I observations (see Walter et al. 2008) with the spectrum calculated from simulations. In this study, it was found stellar feedback processes were needed to recreate the observed power-law slopes.

In the last several years, it is becoming increasingly computationally viable to run cosmological simulations which include radiative transfer (RT; see e.g. Rosdahl et al. 2013; Kannan et al. 2019). Running such simulations, particularly on larger volumes takes a significant number of CPU hours. The other drawback to these simulations is they tend to have a severely limited spectral resolution, i.e. only having  $N$  wavelength bins, where  $N$  is normally between 1 and 10 (e.g. Rosdahl et al. 2018, used 3 bins which covered wavelengths between 0 and  $910 \text{ \AA}$ ). Thus, these kinds of RT-cosmological simulations can provide insight into the number of photons in a given wavelength range however they are unable to provide information about the shape and position of emission features. This makes creating line-of-sight velocity or velocity dispersion maps more difficult. Additionally, all the parameters of an RT simulation, such as the assumed shape of the star’s spectral energy distribution (SED), is set before run time and exploring how the choice of SED would affect the observation of the simulated galaxy requires re-running the simulation, adding to the computational cost. For a more holistic view of RT simulations, we direct the read to Iliev et al. (2009).

One way to gain higher spectral resolution and be able to test how changing the parameters affect observability is to employ a post-processing pipeline to ‘paint’ photons into the simulation after runtime. In Grisdale et al. (2021), we employed such a pipeline to explore the likelihood of detecting Population III stars with the ELT. We were able to show that if such stars have top heavy initial mass function (IMF) detection would be possible.

The High Angular Resolution Monolithic Optical and Near-infrared Integral field spectrograph (HARMONI) will be the work-

horse spectroscopic instrument on ELT, providing spectra from  $0.47$  to  $2.45 \mu\text{m}$  (Thatte et al. 2014). This relatively large wavelength range and its high spatial resolution coupled with the large primary mirror of the ELT, makes it even more important to ensure we are able to accurately interpret observations and decode the properties of the emitting object. It is here that processing simulations with pipelines, such as the one described used in Grisdale et al. (2021), can be extremely powerful.

The primary goal of this work is to explore how the physical properties of a galaxy can be *accurately* recovered from (simulated) observations of emission lines produced in the galaxy. To that end we make use of the hydrodynamical simulation post-processing pipeline LCARS (Light from Cloudy Added to RAMSES) to convert properties, such as the SFR and gas kinematics, into photons which can then be ‘observed’ using the HARMONI simulator (HSIM) before being analysed. In Section 2, we outline LCARS as well as the simulation suite used in this work. We present our galaxy selection criteria, chosen galaxy and its intrinsic properties in Section 3, while Section 4 explores the measured properties of this galaxy after being observed. We discuss implications of spatial resolution, whether photons are a good tracer for gas properties and the meaning of  $v_\theta/\sigma$  in the new high spatial resolution observation paradigm in Section 5. Section 6 presents a summary of this work and its conclusions.

## 2 METHOD

### 2.1 Simulation data set: NEWHORIZON overview

In this work we have selected a simulated galaxy (see Section 3 for details of this galaxy) from the NEWHORIZON simulation. NEWHORIZON is a hydrodynamical, cosmological simulation run using the hydro- $N$ -body, Adaptive Mesh Refinement (AMR) code RAMSES (Teyssier 2002) targeting a linear spatial resolution for the smallest cell of  $\Delta x \sim 35 \text{ pc}$ . New levels of refinement are unlocked as the simulation progresses to account for cosmological expansion. Here, we give a very brief overview of the simulation but direct the reader to Dubois et al. (2021) for complete details (see also Park et al. 2019; Grisdale et al. 2021).

NEWHORIZON is a re-simulation of a spherical region with a radius of  $10 \text{ Mpc}$  (comoving) which has been extracted from the Horizon-AGN simulation (Dubois et al. 2014; Kaviraj et al. 2017). The simulation includes physical processes such as star formation, stellar feedback from star particles and active galactic nucleus (AGN) feedback from black hole (BH) particles. However, it does not include explicit radiative transfer. Star formation occurs on a cell by cell basis when a cell’s gas number density is  $\geq 10 \text{ cm}^{-3}$  and temperature  $< 2 \times 10^4 \text{ K}$ , following a Schmidt law (Schmidt 1959). The star formation efficiency per free-fall time is determined by the local gravo-turbulent conditions of the ISM (Kimm et al. 2017). Each star particle has a mass of  $M_\star \geq 10^4 M_\odot$  and is assumed to represent a population of stars following a Chabrier IMF (Chabrier 2005) with lower and upper mass cut-offs of  $0.1 M_\odot$  and  $150 M_\odot$ , respectively. These particles in turn inject momentum ( $3 \times 10^{49} \text{ erg } M_\odot^{-1}$ ) back into the ISM via supernovae explosions occurring  $5 \text{ Myr}$  after each particle forms (Kimm & Cen 2014).

The simulation produces BH particles in cells where both gas and stellar densities are  $> 10 \text{ cm}^{-3}$ . These particles are initialized with a seed mass of  $10^4 M_\odot$ . The mass of the particles can increase through Bondi–Hoyle–Lyttleton accretion and through BH coalescence (capped at the Eddington limit; Hoyle & Lyttleton 1939; Bondi & Hoyle 1944). BH particles inject feedback into their environment via one of two modes, radio or quasar, set by the accretion rate of

gas on to the BH relative to Eddington (Dubois et al. 2012). Dark matter (DM) particles are also included in the simulation, modelled as collision particles with a mass of  $10^6 M_\odot$ .

## 2.2 Light from CLOUDY added to RAMSES (LCARS)

In Grisdale et al. (2021), henceforth G21, we introduced a post processing pipeline that added photons into RAMSES simulations such as NEWHORIZON. This pipeline took the properties of star particles and gas within the simulation and combined these with a large number of radiative transfer simulations using the microphysics code CLOUDY (see Ferland et al. 2017, for full details on CLOUDY) to determine the shape and magnitude of an emission line along each line of sight. In this work, we make use of an improved version of this pipeline. We refer to this pipeline as ‘Light from Cloudy Added to RAMSES’ or LCARS.

### 2.2.1 Single ‘Super’ star particle in cell approach

The previous version of LCARS (see G21) required running a grid of CLOUDY simulations that covered all possible combinations of cell properties and stellar properties. Each star particle was then matched to the CLOUDY simulation that best matched it and its host cell. For cells with multiple particles, each particle was treated as if it was the *only* one within its host cell when matching to CLOUDY. The final spectrum of such a cell was created from the summation of the matched CLOUDY outputs of each individual particle within the cell. In this updated version of LCARS, we assume that all-star particles within a given cell are located at its centre, in one massive ‘super’ star particle (SSP). A unique SED is calculated for each SSP by summing the individual SED of each of its constituent particles. We assume that the SSP is situated at the centre of cell and has removed all gas, via wind and radiation, within the radius,  $r_{\star \text{void}}$ , where

$$r_{\star \text{void}} = \left( \frac{3M_{\text{SSP}}}{4\pi\rho_{0,\star}} \right)^{1/3}, \quad (1)$$

or  $\Delta x \times 0.45$  whichever is smaller. Here,  $M_{\text{SSP}}$  is the mass of the SSP while  $\rho_{0,\star} = 1500 M_\odot \text{pc}^{-3}$  is a constant stellar density.<sup>1</sup> To maintain mass conservation the gas density of the cell must be adjusted to account for the void region surrounding the SSP. This is achieved by evenly distributing the gas mass throughout a spherical shell with a thickness  $r_{\text{shell}} = (\Delta x/2) - r_{\star \text{void}}$  (see Fig. 1). This modified gas density ( $n_{\text{cloud}}$ ) is then used as an input parameter for CLOUDY.

### 2.2.2 Constructing spectra and data cubes

For each cell with an SSP a unique CLOUDY simulation is run. Each of these CLOUDY simulations are run assuming spherical shell of gas surrounding a single primary radiation source (the SSP), as shown in Fig. 1. The input parameters for CLOUDY, listed in Table 1, are set individually for each cell. In addition to the SSP radiation source our CLOUDY simulations also include diffuse light from neighbouring cells (see Section 2.2.4). A background radiation field which mimics the observed cosmic radio to X-ray background, with contributions from the CMB, is also included. This is assumed to be a blackbody with a temperature of  $T_{\text{CMB}} = 2.725(1+z)\text{K}$ .

RAMSES calculates the gas temperature ( $T_g$ ) for each gas cell within the simulation volume at run time. As a result of the

<sup>1</sup>The value  $\rho_{0,\star}$  is derived by dividing the average mass of a star particle by the size of the void region ( $r_{\star \text{void}} = 2 \text{ pc}$ ) used in G21.

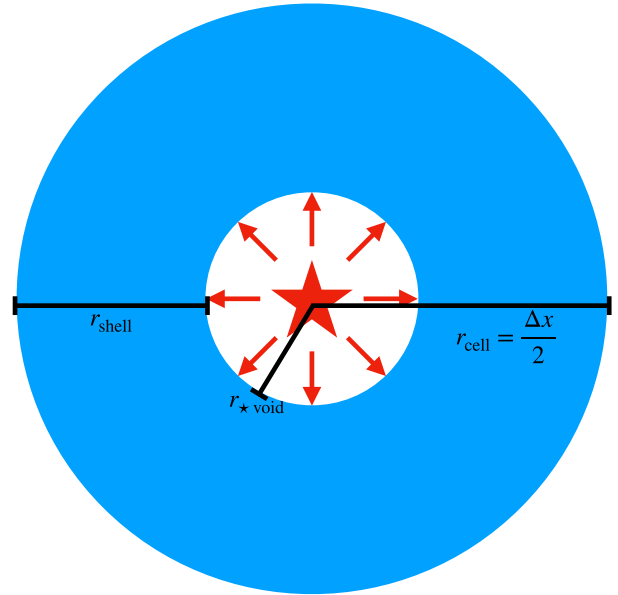


**Figure 1.** 2D depiction of a SSP in a cell. The red star and red arrows represent the SSP and the radiation/wind that has evacuated the void (white) region of gas. The cell’s gas is shown by the blue shell surrounding the SSP. The black lines indicate the scale of each part of the diagram.

**Table 1.** CLOUDY Parameters.

Parameter	Definition
SSP’s SED	Sum of SEDs for star particles within the SSP
$L_{\text{SED, tot}}$	Integral of the SSP’s SED, i.e. SSP’s total luminosity
$r_{\star \text{void}}$	Radius of the gas empty region surrounding SSP
$n_{\text{cloud}}$	Cell’s gas number density (modified for assumed geometry)
$Z$	Metallicity of the gas in cell
$z$	Redshift of the simulation
$r_{\text{shell}}$	Thickness of gas spherical shell, $(\Delta x/2) - r_{\star \text{void}}$
$T_g$	Temperature of the gas (used in certain conditions)

supernovae feedback prescriptions included in NEWHORIZON, there are cells with  $T_g$  in excess of  $10^4 \text{ K}$ , with some reaching a few  $10^8 \text{ K}$  (we refer the reader to Dubois et al. 2021 for full details on the heating and cooling mechanisms within the simulations). We note that only  $\sim 0.003$  per cent, by mass, of G1’s gas has  $T_g \geq 10^8 \text{ K}$ . CLOUDY is unaware of when or where supernovae have occurred and therefore will never predict temperatures  $\gtrsim 2 \times 10^4 \text{ K}$ . As a result CLOUDY will not correctly predict the ionization state of the gas in such hot cells. To address this we employ a temperature threshold: when running CLOUDY models for cells with  $T_g > 2 \times 10^4 \text{ K}$  we enforce a constant temperature equal to  $T_g$ . For the cells below this threshold we allow CLOUDY to determine the temperature. The temperature calculated by CLOUDY is *only* used during CLOUDY’s radiative transfer calculations and not for determining line width.

The strength of each emission line ( $I_0$ ) and the continuum at  $r_{\text{shell}}$ , as calculated by CLOUDY, are then used to construct a spectrum for each cell. First, we assume the emission line is given by

$$I(\lambda) = I_{\text{norm}} e^{-\frac{(\lambda - \lambda_c)^2}{2\sigma_{\text{sim}}^2}}, \quad (2)$$



where  $I_{\text{norm}}$  is a normalization constant ensuring that  $\int I(\lambda) d\lambda = I_0$ ,  $\lambda_c$  is the wavelength of the line in that cell and  $\sigma_{\text{sim}}$  sets the width of the line.  $\lambda_c$  is related to the emission line's rest wavelength ( $\lambda_e$ ) by

$$\lambda_c = \lambda_e \left( \frac{v_{\text{LOS}}}{c} + 1 \right), \quad (3)$$

here  $v_{\text{LOS}}$  is the bulk velocity of the gas within the cell along the line of sight (with respect to the observer). The width of the emission line is set by a combination of both the thermal motions of the gas and velocity dispersion of the gas across the cell, i.e.

$$\sigma_{\text{sim}} = \sqrt{\sigma_{g,\text{therm}}^2 + \sigma_{g,\text{disp}}^2}, \quad (4)$$

where

$$\sigma_{g,\text{therm}} = \lambda_c \sqrt{\frac{k_B T_g}{m_a c^2}}, \quad (5)$$

and

$$\sigma_{g,\text{disp}} = \sqrt{(\sigma_{g,x}^2 + \sigma_{g,y}^2 + \sigma_{g,z}^2)/3}. \quad (6)$$

$T_g$  is the gas temperature in the cell provided by NEWHORIZON,  $m_a$  is the mass of the element emitting the line,  $c$  is the speed of light,  $k_B$  is the Boltzmann constant,  $\sigma_{g,x}$ ,  $\sigma_{g,y}$ , and  $\sigma_{g,z}$  are the gas velocity dispersions of the gas in cell along the three spatial axes of the simulation. The full width at half-maximum (FWHM) of the emission line is related to  $\sigma_{\text{sim}}$  by  $\text{FWHM} = 2\sqrt{2 \ln 2} \sigma_{\text{sim}}$ . The emission line is then added to the continuum<sup>2</sup> calculated by CLOUDY.

Extinction is then applied to the spectrum through

$$I_E(\lambda) = I(\lambda) 10^{\frac{A_V E(\lambda)}{-2.5}}, \quad (7)$$

where  $I(\lambda)$  is the spectrum of a cell before extinction,  $I_E(\lambda)$  is the spectrum after extinction is applied and  $E(\lambda)$  is the dust extinction curve found by Fitzpatrick (1999).  $A_V$  is unique to each cell and given by

$$A_V = 1.086 \frac{3 f_d \Sigma_Z Q_\lambda}{4 \rho_d \sqrt{a_1 a_2}}, \quad (8)$$

where  $\Sigma_Z$  is the column density of metals,  $\rho_d = 3 \text{ g cm}^{-3}$  is the typical density of a dust particle,  $Q_\lambda = 1.5$  is a constant extinction coefficient,  $f_d = 0.01$  is the fraction of gas-phase metals locked up in dust,  $a_1 = 0.005 \mu\text{m}$  is the smallest size of a dust grain and  $a_2 = 1 \mu\text{m}$  is the largest size of a dust grain (see Richardson et al. 2020 for full details of the method and discussion on choice of values).  $\Sigma_Z$  is unique to each cell as it depends on the mass of metals along the line of sight between a cell and the observer.

$f_d$  is a free parameter which can be varied to improve the accuracy of this dust extinction model. With  $f_d = 0.01$ , we find our target galaxy (see Section 3) has an  $A_V$  of 3.44 mag when calculated using a single, galaxy wide spectrum with the methods outlined in Section 4.1.2. Calculating an  $A_V$  map of the galaxy directly from the simulation we find that most extinction line of sight through the galaxy to be  $A_V \sim 22 \text{ mag}^3$  and is located in the densest part of a spiral arm. Increasing  $f_d$  by a factor of 10 leads to values of 7.46 mag and  $\sim 224 \text{ mag}$ , respectively. From observations, it could be argued that a value of 0.2 is more reasonable (Peeples et al. 2014); however, we

find  $f_d = 0.01$  to produce a more realistic  $A_V$  value for a  $z = 2$  galaxy (see e.g. Kahre et al. 2018).

Extinction due to the gas within the current cell is not included as this is applied by CLOUDY. As in G21, we note that the above extinction model is rather simple and does not account for every process that is able to reduce the strength of an emission line or spectra. So that the impact of extinction can be explored a second cube of each line is produced which does *not* include the extinction.

To produce a spatial-spectral cube (SSC), we sum the spectra from all cells along sight line. Finally, the wavelengths of the SSC are redshifted to match the value of  $z$  of the simulation at the time of observation, and the SSC is divided by  $4\pi D_L^2 \delta a^2$  to account for the luminosity distance ( $D_L$ ) and the size of the cell in arcseconds ( $\delta a$ ). The produced SSC has units of  $\text{erg s}^{-1} \text{cm}^{-2} \text{\AA}^{-1} \text{arcsec}^{-2}$ .

### 2.2.3 Constructing spectra for cells without stars

In Sections 2.2.1 and 2.2.2, we limited the discussion to cells that contains star particles. However, in any sufficiently large volume extracted from NEWHORIZON there are cells which do not contain any star particles or diffuse emissions from neighbouring cells (see Section 2.2.4). For these cells, we run a grid of CLOUDY simulations varying  $n_{\text{cloud}}$  and  $Z$  (see Table 1) to cover the range of possible values found in these cells. Given the lack of photons to provide heating and that the majority of these cells are found within the hot Circumgalactic Medium (CGM) or hot (supernova heated) bubbles, to ensure the best match between CLOUDY and NEWHORIZON, we opt to also include  $T_g$  as a third parameter in the grid of CLOUDY simulations. These CLOUDY simulations still assume a spherical shell geometry but with  $r_{\text{void}} = 0$  and  $r_{\text{shell}} = \Delta x/2$ . Furthermore, the incident radiation field used in these simulations is just the background radiation field described in Section 2.2.2. The spectrum in these cells is constructed and added to the SSC in an identical manner to those containing an SSP.

### 2.2.4 Diffuse light from neighbouring cells

We use the radius of the hydrogen Strömgren sphere (Strömgren 1939), i.e.

$$R_{\text{SS,H}} = \left( \frac{3 Q_H}{4\pi n_H n_e \alpha_{B,H}} \right)^{1/3}, \quad (9)$$

as a measure of the fraction of light from a given SSP that has escaped its host cell. Here,  $Q_H$  is the number of photons per second with sufficient energy to ionize hydrogen,  $n_H$  is the number density of hydrogen,  $\alpha_{B,H}$  is the hydrogen recombination rate, and  $n_e$  is the number density of electrons. Both  $n_H$  and  $n_e$  are taken from the simulation and not account for  $r_{\text{void}}$ . If  $R_{\text{SS,H}} \leq 0.5 \Delta x$ , we assume that all ionizing photons interact with the gas in the host cell of the SSP.

In the case of the NEWHORIZON galaxy described in Section 3, we find that  $\sim 18$  per cent of SSPs have a  $R_{\text{SS,H}} > 0.5 \Delta x$ , LCARS therefore needs to be able to account for photons from one cell being deposited into the neighbouring cells. For each SSP with  $R_{\text{SS,H}} > 0.5 \Delta x$ , this is achieved by

- (i) Identifying and tagging all cells which intersect with the Strömgren sphere of the emitting SSP as 'contaminated'.
- (ii) The fraction ( $f_{\text{SS}}$ ) of the Strömgren sphere's volume contained within each contaminated cell is calculated.
- (iii) The SED of the emitting SSP is multiplied by  $f_{\text{SS}}$  and added to the contaminated cell.

<sup>2</sup>Before addition the continuum is Doppler shifted to account for  $v_{\text{LOS}}$ .

<sup>3</sup>When calculating the  $A_V$  map we take the value of  $A_V$  straight from equation (8). Calculations of extinction from the LCARS SSC use the spectrum of the entire galaxy that results in information about extinction as function of depth being lost.

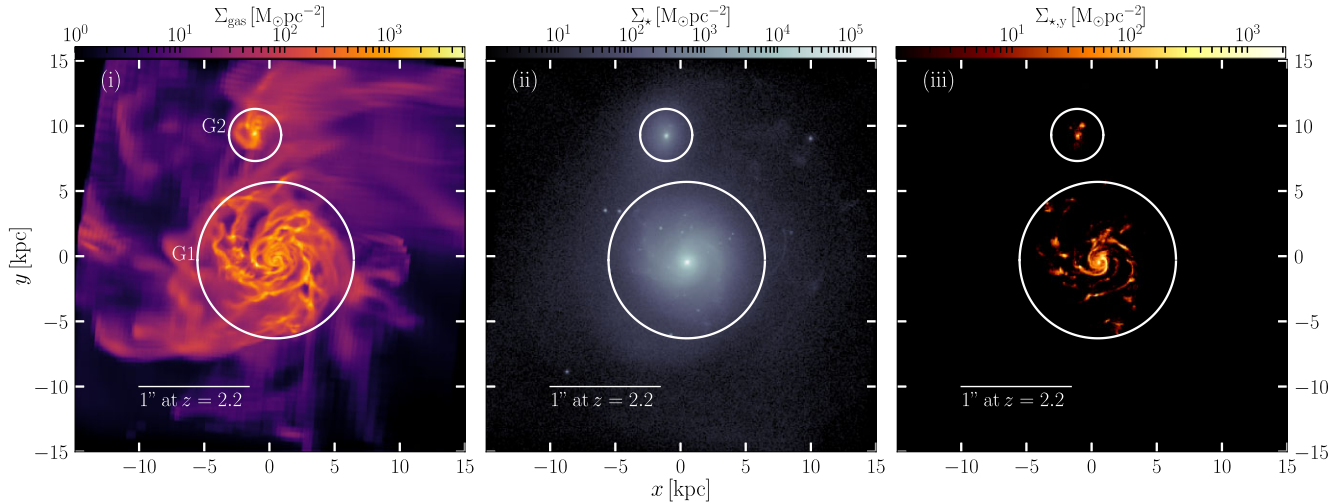


**Figure 2.** Surface density maps for G1 and G2, calculated directly from the simulations. The large white circle indicates the primary galaxy (G1), while the small white circle shows the position of the merging companion galaxy (G2). These two circles have radii of 6 kpc and 2 kpc, respectively. Panels (i)–(iii) show the gas surface density ( $\Sigma_{\text{gas}}$ ), stellar surface density ( $\Sigma_{\star}$ ), and the young stellar surface (i.e. stars with ages  $\leq 10$  Myr) density ( $\Sigma_{\star,y}$ ).

(iv) The SED added to each contaminated cell is subtracted from the SED of the emitting SSP.

(v) Results from (iii) and (iv) are stored, while the original SED of both the contaminated and emitting cells remain unchanged.

(vi) Once all SSP's with  $R_{\text{SS,H}} > 0.5\Delta x$  are identified and the contamination of all cells is calculated, the SED of each cell is updated to account for both contamination and leaked light.

Steps iv–vi ensure that the total energy of each SED is conserved during the diffusion calculation. Any cell that does not contain a SSP but is contaminated by a neighbouring cell is flagged and treated as if it does contain a SSP with the SED set purely by the contamination. More simply, the shape of the SED of such a contaminated cell is the sum of all SEDs contaminating that cell.

This method to account for diffuse light is only a first-order approximation, since it does not account for differences in the gas density of a contaminated cell compared to the emitting cell and the resulting change in the Strömgren sphere. Furthermore, we use the hydrogen Strömgren sphere as our marker for photons escaping the host cell, which neglects the fact that different elements will be ionized out to a different radius from the ionizing source, i.e. each element will have different-sized Strömgren spheres. In this work, we are focused solely on hydrogen emissions lines making the hydrogen Strömgren sphere an excellent proxy.

### 2.2.5 Choice of SED

In order for the SED of a SSP to be created, we required SEDs for each of its constituent star particles. To that end, we employ STARBURST99 (see Leitherer et al. 1999 for details) to generate a range of different SEDs which cover the metallicity and age of the star particles found in NEWHORIZON.

We create SEDs with STARBURST99 by assuming a stellar population with an initial mass of  $10^5 M_{\odot}$  and the same Chabrier IMF used by NEWHORIZON at runtime. By allowing the stellar population to evolve following the Geneva Standard evolution tracks, for a given metallicity, STARBURST99 produces SEDs for a given population at ages between  $10^4$  and  $10^{9.7}$  yr. We generate one set of SEDs for each of the five different discrete metallicities offered by STARBURST99.

At runtime LCARS matches each star particle to the SED closest in age and metallicity. As star particles formed in NEWHORIZON have a variety of birth masses ( $M_{\star,\text{birth}}$ ), it is necessary to scale the magnitude of the SED by  $M_{\star,\text{birth}}/10^5$ . This produces the same result as running STARBURST99 with individual values of  $M_{\star,\text{birth}}$ .

## 3 GALAXY SELECTION AND PROPERTIES

The majority of our analysis is carried out when simulation has run for  $\sim 3.4$  Gyr (i.e. when the simulation has reached  $z \sim 2$ ) by extracting a cubic volume, centred on our galaxy of choice. The sides of this volume all measure 30 kpc across. At  $z = 2$ , the simulation has maximum spatial resolution of  $\Delta x \sim 45$  pc; however, we carry out our analysis (unless otherwise stated) at one level below the maximum refinement (i.e.  $\Delta x \sim 90$  pc) to reduce the computation cost of when running LCARS. At runtime  $\sim 89$  per cent (by mass) of the galaxy's dense gas ( $n_{\text{H}} \geq 1 \text{ cm}^{-3}$ ) is resolved to at least this resolution, with  $\sim 71$  per cent being resolved to the maximum resolution. We rotate our selected galaxy before analysis so that its inclination angle ( $i$ ) is  $20^\circ$ . We define the inclination angle so that  $i = 0^\circ$  corresponds to the angular momentum vector of the galaxy is pointing along the  $z$ -axis of the simulation and towards the reader. For  $i \neq 0$ , the rotation occurs about the  $x$ -axis of the simulation, which is the same as the  $x$ -axis used in Fig. 2.

From NEWHORIZON, we selected a galaxy whose properties are consistent with those of observed on the MS at  $z \sim 2$ , i.e. has a stellar mass ( $M_{\star}$ ) and SFR consistent with galaxies at this redshift. We use the observational sample in our companion work H21 to determine a suitable range of values in  $M_{\star}$  and SFR. Our selected galaxy is presented in Fig. 2 and a summary of its intrinsic properties is given in Table 2. From Fig. 2, it is clear that our selected galaxy is interacting with a smaller galaxy. We refer to these two galaxies as G1 and G2, respectively. We note that it was not intentional to select a galaxy undergoing a merger. Given the ratio of their mass,  $\sim 5$  per cent (see the third column of Table 2), we classify the merger of G1 and G2 as minor. From a visual inspection, G1 appears to be spiral galaxy with two large arms and several small arms. In contrast G2 is comprised of a dense core with two circular gas filaments that extend above and below the galaxy. We define young stars as those

**Table 2.** Summary of galaxy properties.

Property	G1	G2	G2/G1 (per cent)
$\log_{10}(M_{\text{gas}} [\text{M}_{\odot}])^1$	10.2	9.3	12.6
$\log_{10}(M_{\star} [\text{M}_{\odot}])^2$	10.7	9.4	5.0
$\log_{10}(M_{\text{B}} [\text{M}_{\odot}])^3$	10.9	9.6	5.0
$\log_{10}(M_{\text{DM}} [\text{M}_{\odot}])^4$	10.7	9.3	4.0
$\log_{10}(M_{\text{Tot.}} [\text{M}_{\odot}])^5$	11.4	9.8	5.0
$\text{SFR} [\text{M}_{\odot} \text{ yr}^{-1}]^6$	38.3	1.95	5.1
$r [\text{kpc}]^7$	6	2	33.3

Notes. Row 1: gas mass, Row 2: stellar mass, Row 3: total baryonic mass, Row 4: dark matter mass, Row 5: total mass, Row 6: SFR for the last 10 Myr of runtime, Row 7: radius at time of analysis.

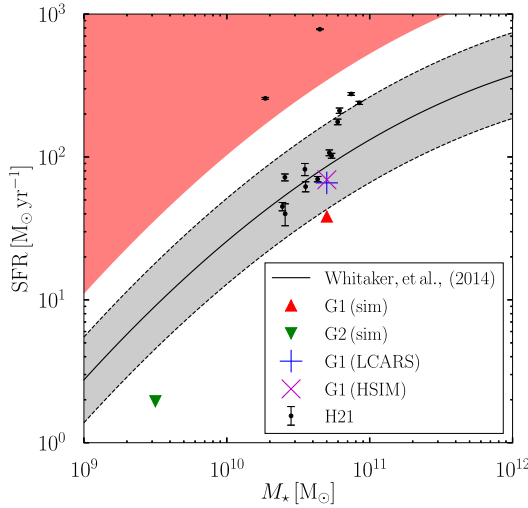


**Figure 3.** The SFR position of G1 (red triangle) and G2 (green triangle) relative to the SFR-stellar mass main sequence as measured directly from the simulation. The black-solid line shows the main sequence for  $2.0 \leq z \leq 2.5$  (as described by equation 2 of Whitaker et al. 2014). The grey shaded regions show values within  $\pm 0.3$  dex of the main sequence. The red shaded region shows where galaxies considered to be ‘starburst’ are found. Observational SFR calculated from IR luminosity data given in Table 3 of H21 are shown by black-circular points. The blue ‘+’ and magenta ‘x’ show the measured SFR of G1 after being passed through LCARS and then HSIM (see Section 4.2), respectively.

with ages less than or equal to  $t_{\star,y} = 10$  Myr. We plot the positions of all young stars in panel (iii) of Fig. 2 that shows that the majority of G1’s star formation is occurring along the lengths of its arms, while G2 is predominantly forming stars in two central clusters. Comparing panels (ii) and (iii) shows that older stars are more evenly distributed throughout both galaxies.

G1 has an SFR of  $\sim 38.3 \text{ M}_{\odot} \text{ yr}^{-1}$  at  $z = 2$ , putting it within  $\sim 0.35$  dex of the galaxy star formation MS as defined in Whitaker et al. (2014, see Fig. 3). For direct comparison with observed  $z = 2$  galaxies, we include the values calculated for 14 galaxies by H21. The evolution of G1’s average SFR per 10 Myr ( $\langle \text{SFR} \rangle$ )<sup>4</sup> is shown in the top panel of Fig. 4. G1 has a very bursty star formation history. Such a

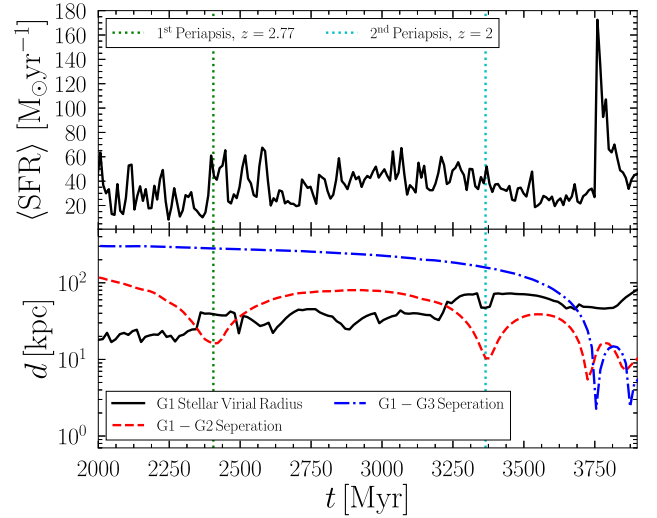


**Figure 4.** Top: Evolution of the mean SFR per 10 Myr for G1 ( $\langle \text{SFR} \rangle$ ). Bottom: Evolution of the separation between G1 and its two satellite galaxies and the virial radius of G1’s stellar component. The two vertical lines running through both panels indicate the first and second periaapsis, with the latter being the time at which we analyse the simulation.

bursty SFR is expected for the star formation prescription employed in NEWHORIZON (see Grisdale 2021). At the time of our analysis ( $z = 2$ ) G1 is undergoing a small burst in  $\langle \text{SFR} \rangle$ , we note that despite this burst the galaxy is not a ‘starburst’ galaxy. From the NEWHORIZON merge tree, we are able to determine that at  $z = 2$ , G2 has completed a single complete orbit of G1, and is currently at periaapsis of its second orbit (see the bottom panel of Fig. 4). At G2’s first periaapsis there is a noticeably larger increase in  $\langle \text{SFR} \rangle$  than at second periaapsis, which might suggest a larger impact cross-section during the initial approach. At  $t = 3750$  Myr, the  $\langle \text{SFR} \rangle$  jumps to  $\sim 180 \text{ M}_{\odot} \text{ yr}^{-1}$ , from the merger tree and based on a visual analysis of the simulation we see that this corresponds to a near head on collision with a third galaxy (which we refer to as G3). After the initial interaction between G1 and G3, G3 is trapped both within the stellar virial radius and the stellar disc of the G1. In contrast, it is not until after the second periaapsis that G2 is trapped within the stellar virial radius. In future work, we will explore the impact of G3 on G1’s evolution further.

By determining the mass enclosed ( $M(R)$ ) within a given galactic radius ( $R$ ) for each of the constituent mass components (i.e. gas, stars, DM, and BH) of the galaxy, their circular velocity ( $v_{\text{circ},i} = \sqrt{GM_i(< R)/R}$ ) is calculated and presented in Fig. 5. Also calculated is  $v_{\text{circ.Tot.}}$ , where  $M_{\text{Tot.}}(< R) = M_{\text{star}}(< R) + M_{\text{gas}}(< R) + M_{\text{DM}}(< R) + M_{\text{BH}}(< R)$ . Comparing  $v_{\text{circ.}}$  of the various components reveals that for  $R < 6$  kpc  $v_{\text{circ.Tot.}}$  is dominated by the stellar mass component of G1 while at larger  $R$  DM is dominant. This change in dominant component is in excellent agreement with the visually assessed edge of G1’s disc at  $R = 6$  kpc. The gas component of G1 has little impact on  $v_{\text{circ.Tot.}}$ . Due to the near negligible effect that BH has on  $v_{\text{circ.Tot.}}$ ,  $v_{\text{circ., BH}}$  is not included in the figure.

Fig. 5 also includes the mean rotational ( $\langle v_{\theta} \rangle$ ) and radial ( $\langle v_r \rangle$ ) velocities<sup>5</sup> of the gas in G1 as a function of  $R$ . Within G1 (i.e.  $R < 6$  kpc)  $\langle v_r \rangle$  is consistent with  $0 \text{ km s}^{-1}$  (with gas moving both towards and away from the galactic centre) while  $\langle v_{\theta} \rangle$  largely agrees with  $v_{\text{circ.Tot.}}$ . This indicates that G1 is a rotationally supported disc

<sup>4</sup>The calculation of  $\langle \text{SFR} \rangle$  does not account for stars that were formed in G1 but subsequently ejected or remove stars that formed in a satellite of G1 before a merger. Therefore,  $\langle \text{SFR} \rangle$  provides an estimate and the general trend of star formation at a given time rather than the precise value.

<sup>5</sup>Both  $v_{\theta}$  and  $v_r$  are polar velocities and should not be compared with spherical velocities.

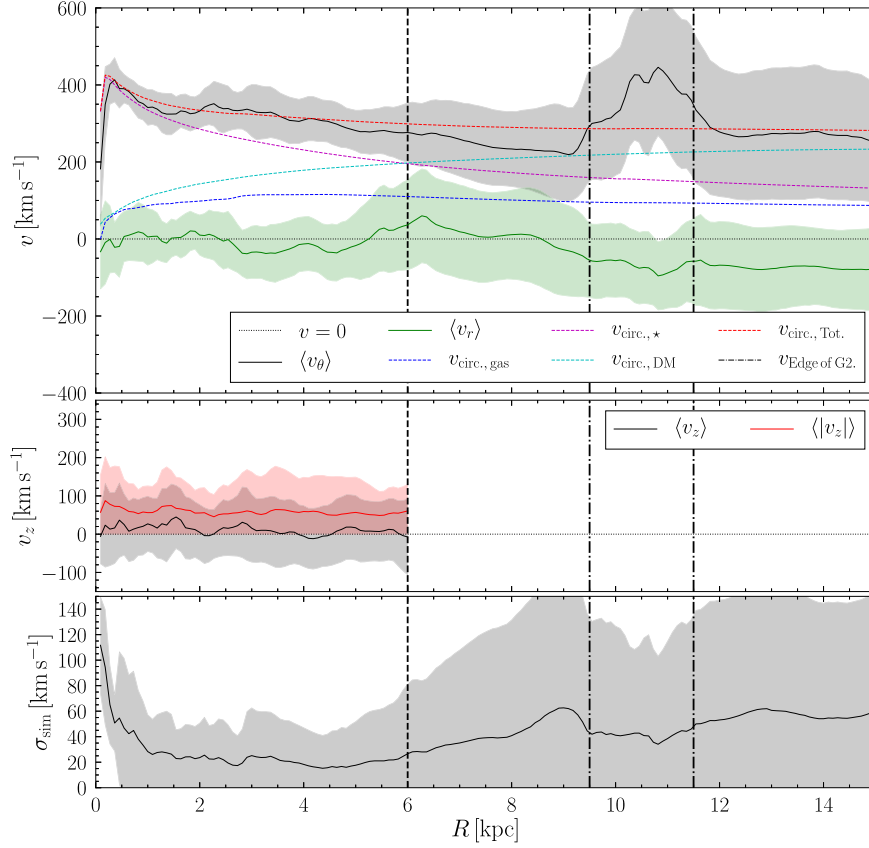


**Figure 5.** Radial mean velocity profiles as a function of  $R$ . Top: Dashed lines show the expected circular velocity for each mass component: DM (cyan), stars (purple), gas (blue), and combined (red). The solid green and black lines show mean radial ( $\langle v_r \rangle$ ) and rotational ( $\langle v_\theta \rangle$ ) velocities for the gas. Middle: Gas velocity perpendicular to G1's disc ( $v_z$ ). The black line shows the mass weighted average of  $v_z$ , while the red line shows the mass weighted average of the magnitude of  $v_z$ . By definition  $v_z$  does not extend beyond edge of G1; therefore, we do not show  $v_z$  for  $R > 6$  kpc. Bottom: The mean radial profile of the velocity dispersion,  $\sigma_{\text{sim}}$ , see Section 2.2.2 for details. All: The shaded regions show  $\pm$  one standard deviation from the mean. The vertical dashed line represents the edge of G1, while the dot-dashed line shows the edge of G2.

as one might expect from a visual inspection of its morphology (see Fig. 2). In Section 4.3 we attempt to quantitatively determine to what extent G1 is a disc. Outside of the G1,  $\langle v_\theta \rangle$  shows a substantial ‘bump’ between  $R \sim 9$  and  $R \sim 12$  kpc, this feature corresponds to G2. For  $R \gtrsim 9$  kpc we find that  $\langle v_r \rangle$  begins to decrease before stabilizing at  $\sim -69$  km s $^{-1}$  which indicates that G1 is accreting gas from these larger radii (including G2).

Completing the triplet of the cylindrical velocity components, the middle panel of Fig. 5 shows the (mass weighted) mean vertical velocity of G1. When accounting for the direction of gas movement,  $\langle v_z \rangle$  tends to be between 0 and 20 km s $^{-1}$ . In a handful of radii gas moving out of the ‘bottom’ of G1’s disc is the more dominant direction of gas flow. Ignoring the direction of  $v_z$  and just focusing on the magnitude, we find that  $\langle |v_z| \rangle$  tends to  $\sim 60$  km s $^{-1}$  at all radii. Therefore at any given radii,  $v_\theta$  is the dominant velocity component of the vast majority of G1’s gas. A visual inspection of G1 reveals the presence of (small) outflows and fountains which is not surprising, given the dispersion on both  $\langle v_z \rangle$  and  $\langle |v_z| \rangle$ .

The mean radial profile of  $\sigma_{\text{sim}}$  is presented in the lower panel of Fig. 5. For G1, we find the (mass weighted) mean  $\sigma_{\text{sim}}$  of  $\sim 23$  km s $^{-1}$ . This value excludes the central kiloparsec, which can have up to  $\times 5.4$  higher  $\sigma_{\text{sim}}$ . The high values in the galactic centre are easily explained by the larger number of young stars and the galaxy’s central massive BH injecting energy in to the surrounding

gas. At radii outside of G1 the mean of  $\sigma_{\text{sim}}$  increases to  $\sim 64$  km s $^{-1}$ , with some features in the profile around G2.

Taking all of the above into account and combining it with visual inspections of the disc, we are able to conclude that the gas of G1 is gravitationally bound, but supported against collapse by galactic rotation. For individual regions within the galaxy,  $v_r$ ,  $v_z$  or turbulence ( $\sigma_{\text{sim}}$ ) can dominate over  $v_\theta$  which can result in outflows, fountains and star formation.

## 4 RESULTS

The following sections compare the galaxies intrinsic properties to those measured from the SSC created by LCARS, including the SFR and rotational velocity of the galaxy. We define ‘intrinsic properties’ to be the values of a given property (e.g. stellar mass) of the galaxy measured directly from the simulation without adding photons, while ‘observed properties’ are the value of the same property determined from mock observations after photons have been added by LCARS. For the purposes of this work, the intrinsic properties are analogues to the physical properties that a galaxy in the physical Universe would have, while observed properties are those that would be derived from observations.

At  $z = 2$ , the wavelength of H  $\alpha$  falls edge of the  $K$ -band grating used by HARMONI. To avoid a loss of data, we artificially move both



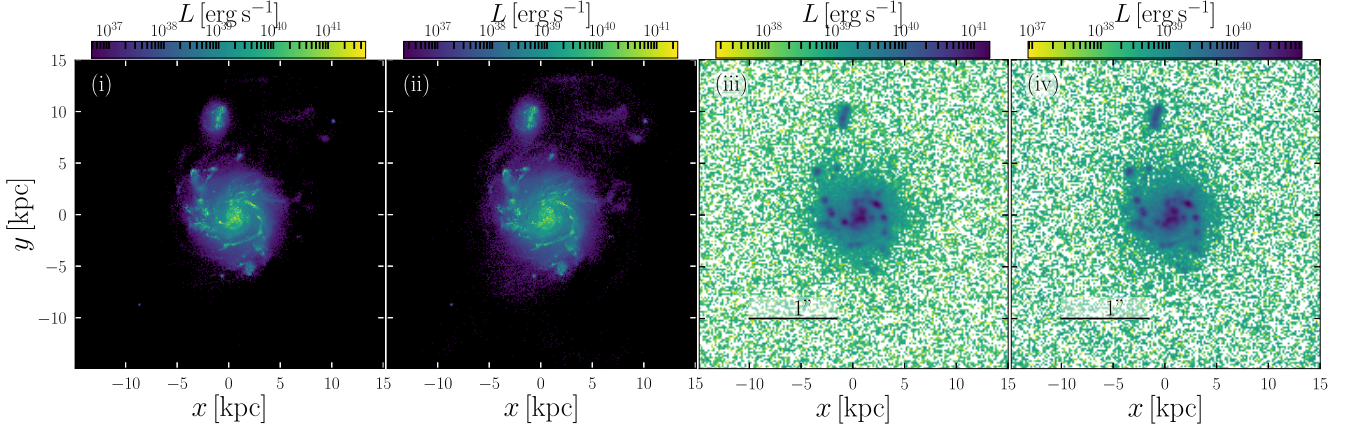


**Figure 6.**  $H\alpha$  zeroth moment maps. The panels show (i) post-LCARS, pre-HSIM, no extinction, (ii) post-LCARS, pre-HSIM, with extinction. (iii) post-LCARS, post-HSIM, no extinction, (iv) post-LCARS, post-HSIM, with extinction. Continuum emission has not been subtracted so as to provide a clear indication of how such a galaxy is likely to appear before analysis.

G1 and G2 to  $z = 2.2$ . This only changes the observed wavelength of the  $H\alpha$  emission line to  $2.1\ \mu\text{m}$  and the value of  $D_L$ . This does not affect the results or conclusions drawn in this work.

#### 4.1 Post-LCARS, pre-observation

We begin our analysis by presenting the results of passing a  $30 \times 30\ \text{kpc}^3$  volume from NEWHORIZON, centred on G1, through LCARS. As stated in Section 3, the extracted volume is passed to LCARS with a fixed spatial resolution of  $\Delta x \sim 90\ \text{pc}$  and results in LCARS running 624 729 unique CLOUDY simulations. Of these, 408 259 are for cells containing SSPs while the remaining 216 470 are for cells contaminated by diffuse emission (see Section 2.2.4).

Throughout this section we focus on the ability to recover the G1's intrinsic properties from the output of LCARS. We leave a discussion of the impact of the telescope (i.e. ELT and HARMONI) on the measured properties until Section 4.2.

##### 4.1.1 $H\alpha$ morphology

From the LCARS SSC, it is possible to calculate the zeroth moment, i.e.  $L = \int I(\lambda) d\lambda$ , of the  $H\alpha$  emission at each spatial pixel location and thus produce the maps shown in panels (i) and (ii) of Fig. 6 that are centred on the  $H\alpha$  emission line. The first of these maps shows the galaxy without any extinction being applied. The post-LCARS maps appear to be an amalgamation of G1's gas and stellar structures. In both maps, the spiral arms are clearly visible and brighter than the more diffuse gas of the disc. Comparing either map from Fig. 6 with the distribution of young stars (i.e. those with ages  $\leq t_{*,y}$ ) in the simulation (see Fig. 2, panel iii) shows that the  $H\alpha$  emission is an excellent tracer of young stars, as expected.

As one might expect, extinction has significant impact on the brightness of G1's spiral arms. As the spiral arms are the primary sites of star formation (other than the galactic centre, see Fig. 2) these are the regions where the brightest pixels are found in the SSCs. The net result of reducing the brightness of the arms is that the diffuse gas between G1 and G2, as well as the gas that is extending towards the right of the maps, appears brighter compared to the arms. Fig. 7 shows integrated emission maps for the  $H\beta$  emission line. Just as with  $H\alpha$  the strongest emission in  $H\beta$  comes from the spiral arms. We note that  $H\beta$  map experiences more extinction than  $H\alpha$  map, as expected.

##### 4.1.2 Measured SFRs

Using a conversion factor it is possible to calculate the SFR of a galaxy from its  $H\alpha$  line emission (Kennicutt et al. 1994). In this work, as in H21, we adopt the conversion

$$\text{SFR}_{H\alpha} [\text{M}_\odot \text{yr}^{-1}] = 5.37 \times 10^{-42} L_{H\alpha} [\text{erg s}^{-1}], \quad (10)$$

from Murphy et al. (2011). Here,  $L_{H\alpha}$  is the integral of the continuum subtracted, single aperture, emission line for the entire galaxy. Using equation (10) with the  $H\alpha$  emissions measured from the SSC without extinction, we calculate  $\text{SFR}_{H\alpha} = 59.1\ \text{M}_\odot \text{yr}^{-1}$ . This is  $\sim 1.54 \times$  the actual SFR of the galaxy.

To calculate the SFR from the  $H\alpha$  SSC with extinction included we first need to correct for the extinction, using

$$L_{H\alpha, \text{emitted}} = L_{H\alpha, \text{observed}} \times 10^{0.4 A_{H\alpha}}, \quad (11)$$

where  $A_{H\alpha} = (3.33 \pm 0.8)E(B - V)$  and

$$E(B - V) = \delta k \log_{10} \left( \frac{(L_{H\alpha}/L_{H\beta})_{\text{observed}}}{2.86} \right), \quad (12)$$

see Domínguez et al. (2013), Osterbrock (1989), and references therein. The pre-factor  $\delta k$  is set by the choice of extinction curve and for consistency we use the same Fitzpatrick curve employed by LCARS (see Section 2.2.2) which gives  $\delta k = 1.50$ . Integrating a single aperture spectrum for both  $H\alpha$  and  $H\beta$  from their respective SSC (which include extinction),  $L_{H\alpha}$  and  $L_{H\beta}$  can be calculated and passed through equations (11) and (12) which gives  $A_{H\alpha} \sim 0.75$ . We then calculate  $\text{SFR}_{H\alpha} = 65.8\ \text{M}_\odot \text{yr}^{-1}$  using equation (10), which is  $\sim 1.72 \times$  larger than the intrinsic SFR of the galaxy. The factor of  $\sim 1.5$ – $1.7$  difference between the intrinsic and measured SFR could come from the choice of  $H\alpha$  to SFR conversion factor, choice, and application of the extinction curve, etc. Given that the measured SFR values do not move G1 off of the MS (see Fig. 3), we argue that these differences are acceptable and that we are able to recover, at least to an order of magnitude the correct SFR of G1. We note that in above calculations only cells that are within a radius of 6 kpc from the galactic centre are considered.

##### 4.1.3 Kinematics structures

In panel (i) of Fig. 8, we show the mass weighted mean value of  $v_{\text{LOS}}$  along the line of sight ( $\langle v_{\text{LOS}} \rangle$ ) map of G1 and G2. Some of the G1's

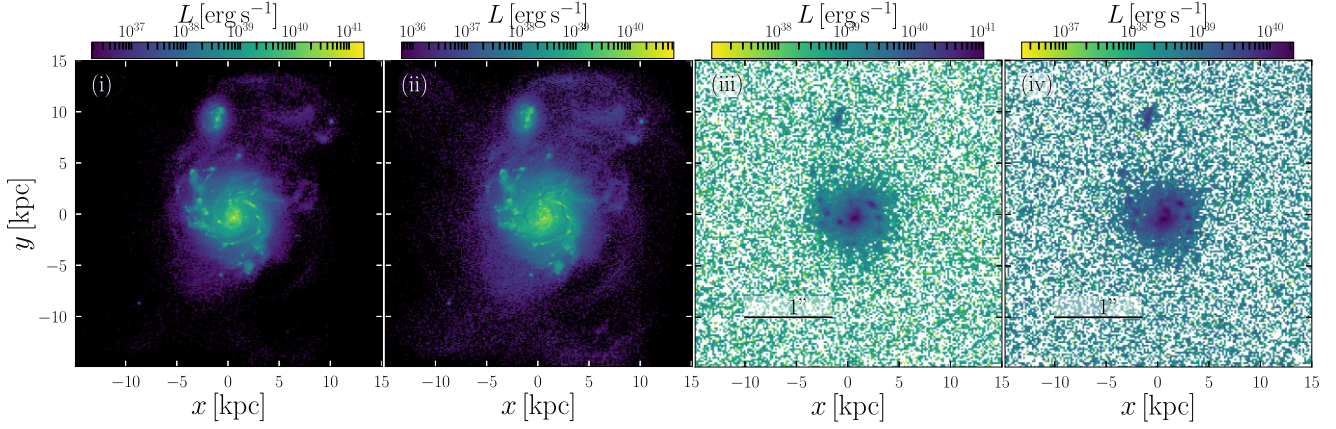


**Figure 7.**  $H\beta$  zeroth moment maps. The panels show (i) post-LCARS, pre-HSIM, no extinction; (ii) post-LCARS, pre-HSIM, with extinction; (iii) post-LCARS, post-HSIM, no extinction; (iv) post-LCARS, post-HSIM, with extinction. Continuum emissions has not been subtracted so as to provide a clear indication of how such a galaxy is likely to appear before analysis.

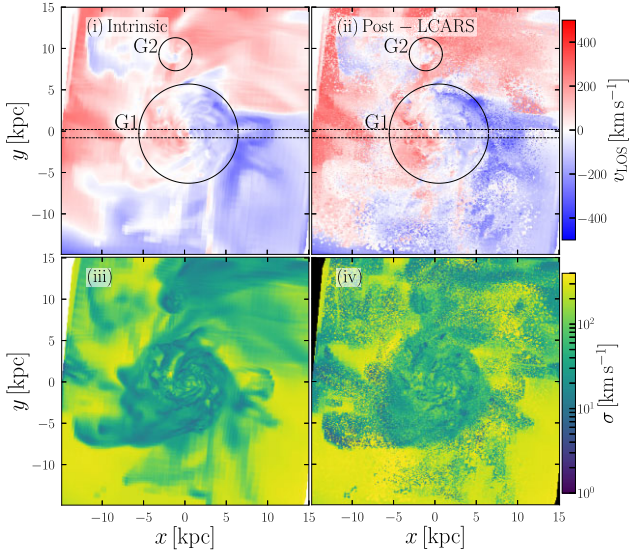


**Figure 8.** Comparison of intrinsic and observational velocity Maps of G1 and G2. Panels (i) and (iii) show the intrinsic line-of-sight velocity and velocity dispersion [ $\langle v_{\text{LOS}} \rangle$  and  $\langle \sigma_{\text{sim}} \rangle_M$ , respectively]. Panels (ii) and (iv) show the first and second moment maps ( $v_{\text{LOS, obs}}$  and  $\sigma_{\text{obs}}$ , respectively) for the SSC produced by LCARS. Continuum is subtracted before  $v_{\text{LOS, obs}}$  and  $\sigma_{\text{obs}}$  are calculated. To aid in comparisons, panels on the same row use the same colour scale which is shown on the right of row. See Section 4.1.3 for definitions of quantities. The dashed horizontal lines show the edges of the slit used for  $v_{\theta, \text{slit}}$  calculations.

spiral structure can be seen in the  $\langle v_{\text{LOS}} \rangle$  maps, though less clearly. From this map, we find that in general,  $|\langle v_{\text{LOS}} \rangle|$  is almost always  $< 500 \text{ km s}^{-1}$  and that the lower density gas found at  $R > 6 \text{ kpc}$  appears to be the most energetic. We also see that the top of G2 is moving away from the observer, while the bottom is moving towards them: i.e. G2 appears to be rotating in the  $y$ - $z$  plane.

In order to determine  $v_{\text{LOS}}$  post-LCARS, we employ the observational method of taking the first moment of the continuum subtract spectrum in each cell, i.e.

$$v_{\text{LOS, obs}} = \frac{\int v_{\lambda} I(v_{\lambda}) dv_{\lambda}}{\int I(v_{\lambda}) dv_{\lambda}}, \quad (13)$$

where  $v_{\lambda}$  is related to wavelength via equation (3) and  $I(v_{\lambda})$  is the intensity in the corresponding velocity (wavelength) channel. The first moment map is shown in panel (ii) of Fig. 8. Within G1 ( $R \lesssim 6 \text{ kpc}$ ) the first moment map agrees with  $v_{\text{LOS}}$  map calculated directly from the simulation, in particular large scale structures match e.g. the gas on the bottom-right side of the galaxy in both maps is moving towards the observer. On smaller scales, within G1, the velocity structures are similar but with some differences in the fine structure (i.e. on scales of  $< 0.5 \text{ kpc}$ ). Perhaps one of the most important difference being that  $|v_{\text{LOS, obs}}| \sim 500 \text{ km s}^{-1}$  is found within the disc of G1 but not in  $\langle v_{\text{LOS}} \rangle$ . We discuss the source of these high velocity regions in the first moment map in Section 5.2. Due to a lack of young, bright,  $H\alpha$ -emitting stars, the spectrum for a given pixel at  $R \gtrsim 6 \text{ kpc}$  is continuum dominated which results in the noisy measurements of  $v_{\text{LOS, obs}}$  shown in Fig. 8

The spiral structure of the G1 is more easily seen in panel (iii) of Fig. 8, which shows the *mass* weighted mean value of  $\sigma_{\text{sim}}$  (as defined in equation 4) along the line-of-sight ( $\langle \sigma_{\text{sim}} \rangle_M$ ) map. This map recovers a lot of the detailed gas structure seen in the gas surface density maps of the galaxy (see Fig. 2). The second moment,

$$\sigma_{\text{obs}} = \sqrt{\frac{\int I(v_{\lambda})(v_{\lambda} - v_{\text{LOS, obs}})^2 dv_{\lambda}}{\int I dv_{\lambda}}}, \quad (14)$$

provides the observational equivalent of  $\langle \sigma_{\text{sim}} \rangle_M$ , though as with  $v_{\text{LOS, obs}}$  this is photon weighted. In panel (iv) of Fig. 8, we show a map of  $\sigma_{\text{obs}}$ . Despite being noisier than the  $\langle \sigma_{\text{sim}} \rangle_M$  map the two maps show broadly the same structure. For example, both maps show that the spiral arms are regions of fairly uniform motion. Some of the details in  $\sigma_{\text{obs}}$  is lost due to noise, i.e. spaxel's with strong continuum relative to the emission.

As the galaxy is inclined at  $i = 20^\circ$ ,  $v_{\text{LOS}}$  contains contributions from both  $v_{\theta}$  and  $v_r$  as well as  $v_z$ . As the position of the emission line for each cell is set by  $v_{\text{LOS}}$  (see Section 2.2.2)  $\langle v_{\text{LOS}} \rangle$  also contains contributions from the  $v_{\theta}$  of each of the cells combined along the line of sight. We apply a slit across the  $v_{\text{LOS, obs}}$  map (shown as dashed lines in Fig. 8). The slit is positioned to run through the centre of G1 and along the inclination axis. For each pixels within this slit, we approximate  $v_{\theta}$  from  $v_{\text{LOS, obs}}$  as

$$v_{\theta, \text{slit}} = \frac{v_{\text{LOS, obs}}}{\sin(i)}. \quad (15)$$



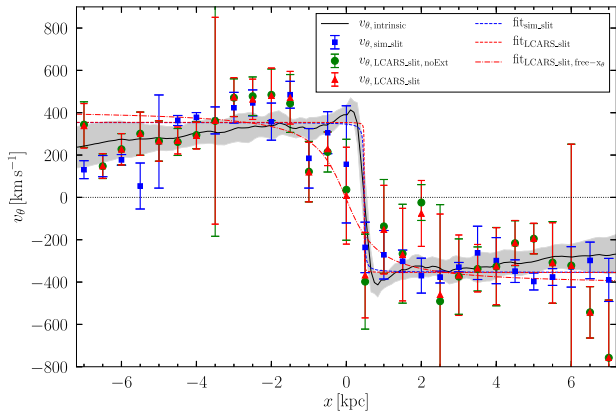


**Figure 9.**  $v_\theta$  profiles calculated from pixels extracted from the slit shown in Fig. 8. The intrinsic rotation curve (solid black line) is included to aid in comparison. The coloured data points represent the weighted mean value of  $v_\theta$  calculated from the slit every 0.5 kpc, while their error bars show the associated weighted  $1\sigma$  value. Blue, magenta, and red data points show values calculated from the  $\langle v_{\text{LOS}} \rangle$  map, the  $v_{\text{LOS,obs}}$  map neglecting extinction, and the  $v_{\text{LOS,obs}}$  map, respectively. The dashed lines represent an arctan fit to data points with matching colour. The dash-dotted line shows an arctan fit to the  $v_{\text{LOS,obs}}$  map, where position of  $x_\theta$  is not known. Note that  $x = 0$  kpc is centre of the map *not* the kinematic centre of the galaxy.

By taking the weighted mean and standard deviation ( $1\sigma$ ) values of  $v_{\theta,\text{slit}}$  every 0.5 kpc along the  $x$ -axis we are able to produce estimates of the rotation curve. We apply the same slit method to the  $\langle v_{\text{LOS}} \rangle$  map to provide a comparison. In the former case pixels are weighted by their integrated line emission, while the latter is weighted by the gas mass of a pixel. The resulting rotation curves are presented in Fig. 9.

We check the validity of calculating the rotations curves from a slit by comparing the slit-calculated curve from  $\langle v_{\text{LOS}} \rangle$  to the intrinsic  $v_\theta$  curve,<sup>6</sup> and we denote those two rotation curves as  $v_{\theta,\text{sim,slit}}$  and  $v_{\theta,\text{intrinsic}}$ , respectively. An exact match between the two is not expected given that  $v_{\theta,\text{intrinsic}}$  is calculated for a significantly larger data set, i.e. the entire galaxy, rather than just a narrow slice through the centre.<sup>7</sup> This means that a small, (abnormally) high/low-velocity region which crosses the slit will have a more substantial impact on  $v_{\theta,\text{sim,slit}}$  than it would have if all cells within that galaxy at that particle radius were included in the calculation. With that said, except for a handful of data points, when  $|x| \leq 6$  kpc we find that  $v_{\theta,\text{sim,slit}}$  is within  $1\sigma$  of the intrinsic value and therefore consistent with  $v_{\theta,\text{intrinsic}}$ . The data points that deviate can easily be explained by small-scale structure seen in panel (i) of Fig. 8. We conclude that the slit calculated curves provide a reasonable estimate of the G1 rotational velocity.

We now turn our attention to the rotation curve calculated from the  $v_{\text{LOS,obs}}$  map,  $v_{\theta,\text{LCARS,slit}}$ . It could be argued that all data point, except the one at  $x = 2$  kpc, are consistent with  $v_{\theta,\text{intrinsic}}$  (when  $1\sigma$  are considered). However, this is in part due to the large values of  $1\sigma$  found for  $v_{\theta,\text{LCARS,slit}}$ . The  $v_{\text{LOS,obs}}$  map in Fig. 8 shows a larger range of values within G1 than seen in the  $\langle v_{\text{LOS}} \rangle$  map. For

example at  $(-2.9, -0.25)$  we see a small (blue) region moving in the opposite direction to its surroundings, which provides an explanation for  $1\sigma \sim 488 \text{ km s}^{-1}$  on  $v_{\theta,\text{LCARS,slit}}$  at  $x = -3.5$  kpc. Furthermore, for  $R > 6$  kpc the large amount of noise in  $v_{\text{LOS,obs}}$  leads to large uncertainty on  $v_{\theta,\text{LCARS,slit}}$  at these radii.

By fitting an arctan profile to both  $v_{\theta,\text{sim,slit}}$  and  $v_{\theta,\text{LCARS,slit}}$ , we are able to quantitatively compare how processing G1 with LCARS has impacted the recovered rotation curve. When fitting we provide the  $x$ -position of the centre of rotation,  $x_\theta = 0.475$  kpc, which is calculated directly from the simulation. We find the asymptotes of the arctan fit to be at  $354 \pm 5$  and  $355 \pm 22 \text{ km s}^{-1}$ , respectively. Both values are a reasonable match to  $v_{\theta,\text{intrinsic}}$  at its flattest part ( $0.5 \lesssim R \lesssim 3.0$  kpc), which we find to be  $\sim 340 \text{ km s}^{-1}$ . The fitted arctan profile also captures the sharp increase in  $v_{\theta,\text{intrinsic}}$  found around the galactic centre.

Assuming that  $v_{\theta,\text{LCARS,slit}} = v_{\text{circ,Tot.}}$  (at  $R = 6$  kpc), we are able to estimate the total mass (i.e. sum of stellar, gas, dark matter, BHs mass) enclosed within G1's disc as  $1.76 \times 10^{11} M_\odot$  from the LCARS H  $\alpha$  SSC. This is  $\sim 1.39 \times$  larger than the actual total mass of G1 (see Table 2). Thus to within a factor of a few we are able to recover the total mass of the G1. The steady decrease in the rotation curve seen at  $R \gtrsim 3$  kpc, which is not modelled by an arctan profile, provides the explanation for the difference between the intrinsic and measured enclosed mass at  $R < 6$  kpc.

If  $x_\theta$  is instead left as a free parameter, the fitted arctan profile does not accurately capture the galactic centre and leads to a larger value of  $v_\theta$  for the asymptote, i.e.  $416.3 \pm 27.2 \text{ km s}^{-1}$ . Estimating the mass of the galaxy from this fit gives an enclosed mass of  $2.42 \times 10^{11} M_\odot$  at  $R < 6$  kpc (i.e.  $1.92 \times$  the true value). Therefore, even if the galactic centre is not known a reasonable, but higher, values of both  $v_\theta$  and the enclosed mass can still be estimated.

In summary, the analysis shows that creating SSCs using LCARS encodes rotational velocity information about galaxy into the emission lines as intended. With prior knowledge of the galaxy (such as inclination or galaxy centre) and an absence of observational effects (e.g. noise and sky lines) the above slit method can be used to extract the rotational curve from a galaxy with reasonable accuracy. Therefore, we argue that this method is useful for testing if  $v_\theta$  has been encoded in the outputs of LCARS but caution its use for actual observational data. In Section 4.2.2, we explore an alternative method which can be applied to observational data.

## 4.2 Post-LCARS, post-observation

The analysis in the previous section was all carried out without accounting for a telescope or spectrograph. In the following section, we pass the SSCs from LCARS through HSIM to produce mock ELT observations of G1. This simulator models all *known* instrumental effects introduced by the HARMONI (we direct the reader to Zieleniewski et al. 2015 for an overview of HSIM). In this work, we employ HSIM v3.03.<sup>8</sup> We summarize our default HSIM ‘observation’ settings in Table 3. These settings are adopted for all ‘observations’ unless stated otherwise. As the primary goal of this work is to explore which physical values of a galaxy can be recovered from observations with HARMONI on the ELT (and by extension other 30 m-class telescopes) the observation settings used have been selected to provide the best possible data from an observation with ideal observational conditions (e.g. no moon).

<sup>6</sup>To aid with the comparison we mirror and flip the intrinsic curve to produce an arctan-like curve which covers the width of the entire slit. Additionally, the curve is shifted horizontally so that  $v_{\theta,\text{intrinsic}} = 0.0$  at the kinematic centre of the galaxy which is found at  $x = 0.475$  kpc.

<sup>7</sup>19 243 854 individual cells are used when calculating the  $v_{\theta,\text{intrinsic}}$  curve compared to the 2497 pixels used in the slit-calculated method.

<sup>8</sup>Details of this version can be found at <https://github.com/HARMONI-ELT/HSIM>.

**Table 3.** hsim Settings.

Parameter	Settings
Exposure time (s)	900
Number of exposures (without extinction)	20
Number of exposures (with extinction)	40
Total exposures time (without extinction)	5 h
Total exposures time (with extinction)	10 h
Spatial pixel scale (mas)	20x20
Adaptive optics mode	LTAO
Zenith seeing (arcsec)	0.57
Air mass	1.1
Moon illumination	0.0
Telescope Jitter sigma (mas)	3.0
Telescope temperature (K)	280
Atmospheric differential refraction	True
Noise seed	10
Grating (H $\alpha$ )	K
Grating (H $\beta$ )	H

We leave exploring how different telescope settings will impact the accuracy of observations to future work.

In this work, we use the ‘reduced’ HSIM output cubes, which contain the simulated observations (with noise) after sky observations have been subtracted. Additionally, we use the accompanying signal-to-noise ratio (SNR) cube ‘reduced\_SNR’ as a means of filtering out spaxels dominated by noise rather than signal from G1.

#### 4.2.1 Morphology and SFRs

Panels (iii) and (iv) of Fig. 6 show the zeroth moment map of the H  $\alpha$  emission line after G1 has been observed with HSIM.<sup>9</sup> While the centre of the galaxy and the two largest spiral arms are still clearly visible, the majority of the structural detail seen in (ii) has now been lost. Even when extinction is neglected, i.e. panel (iii), these details are not recovered. Post-HSIM G1 also appears smaller, with an apparent radius of  $\sim 4$  kpc. G2 is still discernible however it is greatly reduced in size. H  $\beta$  observations (see Fig. 7) show similar change but to a larger degree; i.e. G1’s apparent size is further reduced and G2 is effectively lost in noise. We stress that compared to current observations the level of structure recovered by observations with HSIM, and thus should be recovered with HARMONI, are still significantly better than what is achievable with current telescopes (see the discussion in Section 5.1.2).

We apply an SNR mask to the HSIM outputs to reduce the impact of noise on our measurements of  $\text{SFR}_{\text{H}\alpha}$ , i.e. all spaxels with a  $\text{SNR} < 3$  are masked. As in Section 4.1.2, only spaxels that are within 6 kpc of galactic centre (i.e. only spaxels belonging to G1) are included in  $\text{SFR}_{\text{H}\alpha}$  calculations. Fig. 10 shows the line emission maps after the two masks have been applied. Again taking a single aperture spectrum, carrying out continuum subtraction and applying equation (10) we recover a  $\text{SFR}_{\text{H}\alpha} = 50.9 \pm 0.0009 \text{ M}_{\odot} \text{ yr}^{-1}$  from the extinction free H  $\alpha$  SSC. This value is below the value we measure from the H  $\alpha$  SSC before observation with HSIM ( $\sim 59.1 \text{ M}_{\odot} \text{ yr}^{-1}$ ).

Comparing panels (i) and (ii) of Fig. 10 provides an explanation for this discrepancy: the more extended, inter-arm emissions of G1, is below the SNR cut. Little to no star formation is occurring in the inter-arm spaces (see panel (iii) of Fig. 2); however, due the

diffusion module of LCARS (see Section 2.2.4), these regions contain photons emitted by star-forming regions and thus have integrated H  $\alpha$  luminosities between  $\sim 10^{38}$  and  $\sim 10^{39} \text{ erg s}^{-1}$  which is two or more magnitudes lower than the star-forming arms.

We now turn to the SFR for the SSCs that include extinction. As in Section 4.1.2 the H  $\alpha$  flux needs to be corrected and again we use the H  $\beta$  emission line to estimate the correction. After applying the same SNR and radial masks as above, followed by equations (11) and (12), we compute a single aperture spectrum from which we calculate an  $A_{\text{H}\alpha} \sim 1.036 \pm 0.0001$  and thus a  $\text{SFR}_{\text{H}\alpha} = 69.3 \pm 0.0003 \text{ M}_{\odot} \text{ yr}^{-1}$ . This measured SFR is  $\sim 1.81 \times$  the intrinsic SFR. This value is within 6 per cent of the value obtained directly from the LCARS SSC. We are therefore able to conclude that ELT and HARMONI systematics should not significantly impact the measurement of SFR and that the method used to convert H  $\alpha$  emissions to SFR will be the most important source of any errors in observations.

The uncertainties we report for the observed  $A_{\text{H}\alpha}$  and  $\text{SFR}_{\text{H}\alpha}$  are calculated by propagating the variance cube (i.e. the inverse of the ‘reduced\_SNR’ data cube) through equations (10)–(12). As mentioned previously, we chose to employ the optimal observing conditions for kinematic analysis when carrying out our mock observations. Voxels above the SNR cut which contain signal from an emission line are typically several orders of magnitude stronger than any noise or variance. Consequently, we find very small uncertainties on for both  $A_{\text{H}\alpha}$  and  $\text{SFR}_{\text{H}\alpha}$ . In typical observations, the conditions are likely to be less optimal and therefore higher uncertainties should be expected.

The choice of SNR cut can have an impact on the value of  $A_{\text{H}\alpha}$  which in turn impacts measured SFR. For example, reducing the SNR limit to 2.0 results in a larger  $L_{\text{H}\beta}$  while  $L_{\text{H}\alpha}$  remains approximately constant, this produces a smaller  $A_{\text{H}\alpha}$  ( $\sim 0.72$ ) and thus  $\text{SFR}_{\text{H}\alpha} = 55.89 \pm 0.0006 \text{ M}_{\odot} \text{ yr}^{-1}$ . However, the choice of SNR cut is not as important as how extinction is accounted for and how H  $\alpha$  is converted to SFR. In summary, it is possible to recover the SFR of G1 after observations in within a factor of  $\sim 2$ .

#### 4.2.2 Kinematic structures

We present the kinematic structure of G1 post-HSIM observation in Fig. 11. We again apply a SNR mask to remove contributions from spaxels with  $\text{SNR} < 3$  before applying equations (13) and (14). From the first moment maps [panels (i) and (ii)], we see that generally the  $v_{\text{LOS}}$  structure of G1 is preserved after observation with HSIM. However, there is a further reduction in detailed structure compared with the post-LCARS  $v_{\text{LOS}}$  maps. The second moment maps are also fairly uniform, though there is a peak in  $\sigma_{\text{obs}}$  at the galactic centre. Given how bright (see Fig. 6) and chaotic the galactic centre is (see the lower panel Fig. 5), seeing a high  $\sigma_{\text{obs}}$  in this region is expected.

Passing the LCARS SSCs through HSIM introduces noise and instrumental effects. As a result a slit along the major axis of the galaxy cannot be used reliably to recover the intrinsic  $v_{\theta}$ . By adopting a simple kinematic model, it is possible to estimate the rotational velocity of G1 from HSIM observations. In this case, we adopt equation (1) of Arribas et al. (2008) in the form

$$v_{\text{LOS},\text{mod}}(R, \theta) = \Omega(R) \cos(\theta - \theta_0) \times \sin i + v_{\text{sys}}, \quad (16)$$

where  $R$  is the distance from galactic centre,  $\theta$  is the angle from the major axis,  $v_{\text{LOS},\text{mod}}(R, \theta)$  is the line-of-sight velocity predicted by the model at  $(R, \theta)$ ,  $v_{\text{sys}}$  is the systematic velocity of the galaxy along the line of sight,  $i$  is the inclination angle of the galaxy,  $\theta_0$  is the position angle and  $\Omega(R)$  is a function describing the rotation curve

<sup>9</sup>We have not employed an SNR filter to Fig. 6 so as to provide the reader with a clear expectation of the expected noise when observing a G1-like galaxy with the physical HARMONI on the ELT.



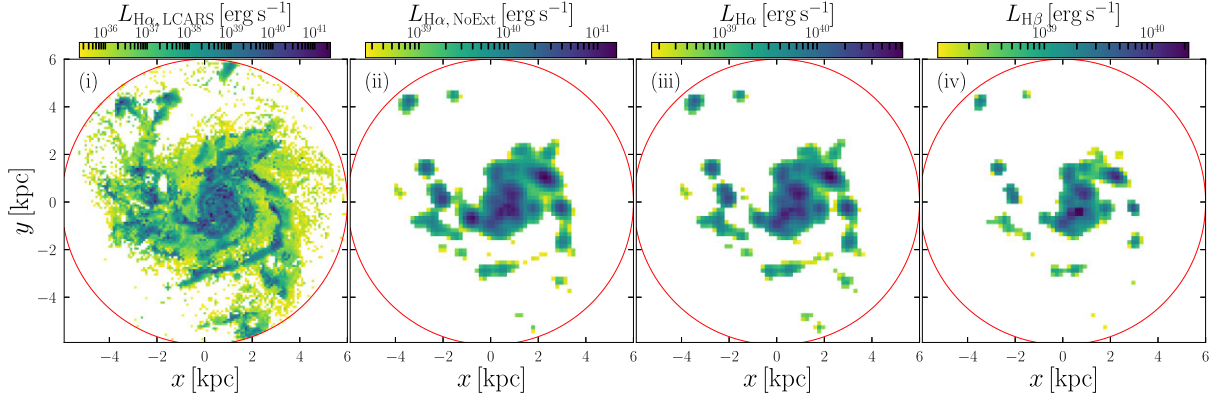


**Figure 10.** Zeroth moment maps after the application of an SNR and radius mask have been applied. Panels (ii)–(iv) show maps created from HSIM output data cubes of: H  $\alpha$  (without extinction), H  $\alpha$  (with extinction), and H  $\beta$  (with extinction), respectively. For these panels only spaxels with  $\text{SNR} \geq 3$  are included in the maps. Panel (i) is the same as panel (ii) in Fig. 6 but zoomed in. The red ring in each panel represents edge of G1 and the radius of the radial mask. Continuum emission has been subtracted from all four panels.

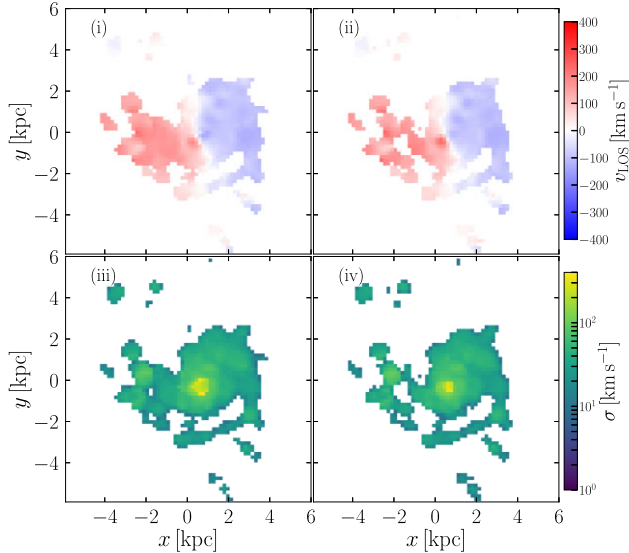


**Figure 11.** First and second moment maps ( $v_{\text{LOS, obs}}$  and  $\sigma_{\text{obs}}$ , respectively) after our H  $\alpha$  SSC have been observed with HSIM. Panels (i) and (ii) show  $v_{\text{LOS, obs}}$  for SSC without and with extinction, respectively, while panels (iii) and (iv) show their respective  $\sigma_{\text{obs}}$ . Continuum is subtracted and an SNR mask is applied before  $v_{\text{LOS, obs}}$  and  $\sigma_{\text{obs}}$  are calculated. To aid in comparisons, panels on the same row use the same colour scale which is shown on the right of row. See Section 4.1.3 for definitions of quantities.

(we again adopt an arctan profile). Fitting the above model to the  $v_{\text{LOS, obs}}$  map shown in panel (ii) of Fig. 11, setting  $i = 20^\circ$ ,  $\theta_0 = 0^\circ$  and letting  $v_{\text{sys}}$ , the asymptote value as well as the gradient of the arctan profile be unknowns, we find the model presented in Fig. 12. In a general sense, the model is able to produce a crude approximation of  $v_{\text{LOS, obs}}$ , but with the bubbles of large  $|v_{\text{LOS, obs}}|$  missing (as expected). From the simulation, it is known that the region with  $v_{\text{LOS, obs}} \gtrsim 200 \text{ km s}^{-1}$  centred around  $(-1, -1)$  of panel (ii) of Fig. 11 is the result of a large number of young stars creating a low density, high velocity, high temperature bubble on the trailer side of the nearest spiral arm. The model presented in equation (16) has no way to include, account for, or recreate stellar feedback driven gas in the model and thus is unable to produce a recreation of the *turbulent*

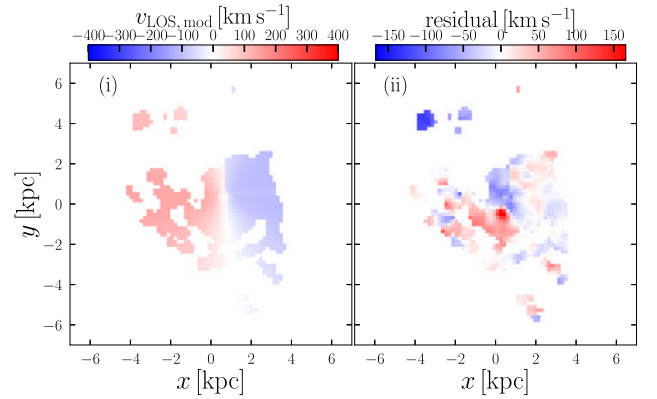


**Figure 12.** Left:  $v_{\text{LOS, mod}}$  map (see equation 16) with model parameters of  $20^\circ$ ,  $0^\circ$ ,  $15.6 \text{ km s}^{-1}$ ,  $365.4 \text{ km s}^{-1}$ , and  $7.005$  for  $i$ ,  $\theta_0$ ,  $v_{\text{sys}}$ , arctan asymptote, and arctan gradient, respectively. Right: Map of residuals between the model and the  $v_{\text{LOS, obs}}$  map [panel (ii) of Fig. 11], i.e. the former subtracted from the latter.

velocity structure of the galaxy. This leads to the large residuals seen in the right-hand panel of Fig. 12.

This model estimates the asymptote of the arctan function, i.e.  $v_\theta$ , to be  $365.4 \pm 5.5 \text{ km s}^{-1}$ , which is slightly larger than the true value of  $\sim 340 \text{ km s}^{-1}$ , but is consistent with the values found from the post-LCARS SSCs (when errors are considered). Given the inability to model the finer structure of a galaxy, we argue that such a model is not ideal for our all of our analysis, e.g.  $v_\theta/\sigma$  calculations see Section 4.3.

We therefore opt to use a more sophisticated model that allows for clumps of gas at given  $R$  to have high dispersion and  $v_{\text{LOS, obs}}$ . In this case, we use the analysis tool <sup>3D</sup>BAROLO (see Teodoro & Fraternali 2015 for details) to extract a rotation curve from the map of  $v_{\text{LOS, obs}}$ . We provide <sup>3D</sup>BAROLO the ‘reduced’ and ‘reduced\_SNR’ data cubes and allow the programme to make its own SNR cuts to the data. In this case, it finds every pixel  $\text{SNR} > 5$  as well as all the  $\text{SNR} > 3$  pixels that are located around the first set of pixels. These regions are joined together if they are side by side. <sup>3D</sup>BAROLO has a plethora of settings and variables that can be left to be determined or fixed. In this work, we focus on 10 of these variables. We start by determining the best settings using our prior knowledge of the

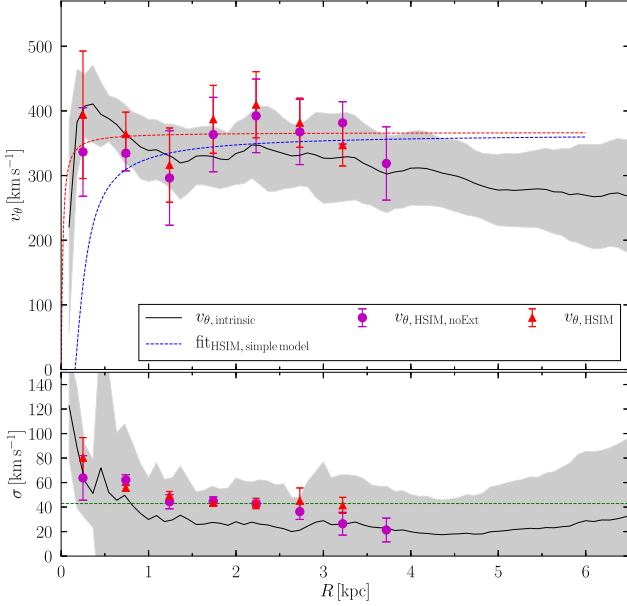


**Figure 13.** Top: Rotational velocity radial profile [ $v_\theta(R)$ ]. The solid black line shows the intrinsic curve for G1. The purple and red points show the values found by  $^3\text{D}\text{BAROLO}$ , using the fiducial fitting parameters for G1 (no extinction and with extinction, respectively) after being ‘observed’ HSIM. The red dashed line shows an arctan fit to the red ( $^3\text{D}\text{BAROLO}$ ) data points, while the blue dashed line shows the arctan fit found by the simple kinematic model (i.e. equation 16). The shaded region represents  $1\sigma$  from the intrinsic curve. Bottom: Velocity dispersion radial profile ( $\sigma(R)$ ) for the same data sets as the top panel.

simulation and use this analysis run as our fiducial results from  $^3\text{D}\text{BAROLO}$ . To calculate errors on this fit we run  $^3\text{D}\text{BAROLO}$  seven additional times, for each of these runs we allow one or more variables to be determined by  $^3\text{D}\text{BAROLO}$ . The variables allowed to be fitted are position angle, inclination angle,  $x$ -position of the galactic centre,  $y$ -position of the galactic centre, systematic velocity, radial velocity, and position angle & inclination angle simultaneously.  $^3\text{D}\text{BAROLO}$  is able to weight the receding or approaching side of the galaxy preferentially or equally. In the fiducial settings we weight them equally.<sup>10</sup> By changing this, we are able to carry out three additional  $^3\text{D}\text{BAROLO}$  analysis runs: receding side preferentially weighted, approaching side preferentially weighted and position angle & inclination angle with the approaching side preferentially weighted. To calculate an error on  $^3\text{D}\text{BAROLO}$ ’s fit, we calculate the standard deviation of the 10 non-fiducial runs from the fiducial run. The resulting rotation curve, with error is presented in Fig. 13. The fiducial  $^3\text{D}\text{BAROLO}$  model is in good agreement with the intrinsic curve.

As before we fit an arctan curve to the  $^3\text{D}\text{BAROLO}$  data points to determine the asymptote of the rotation curve and find a value of  $366.9 \pm 17.3 \text{ km s}^{-1}$ . By repeating our mass estimate, i.e.  $v_{\theta, \text{BAROLO}} = v_{\text{circ, Tot.}} = 366.9 \text{ km s}^{-1}$ , we estimate the total mass enclosed at  $R = 3.25$  to be  $1.017 \times 10^{11} \pm 10^{9.982} \text{ M}_\odot$  or  $\sim 0.81 \times$  the total mass of G1. However, at  $R = 3.25$  the total mass enclosed

<sup>10</sup>When fitting the ‘reduced’ cube produced from the SSC without extinction, we preferentially fit to the approaching side of the galaxy as this provides the best match to the intrinsic rotation curve. This choice is discussed more in Section 5.2.

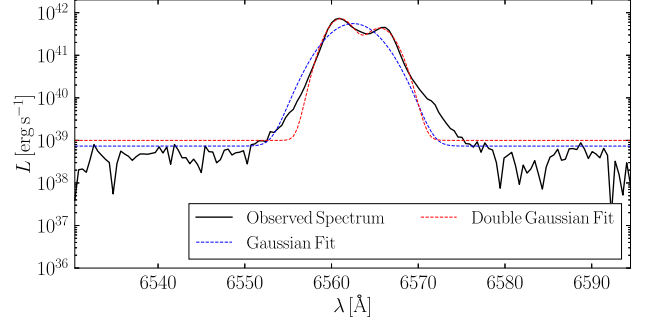


**Figure 14.** Single aperture, continuum subtracted, spectrum of G1 after being observed with HSIM (black line). Dashed lines show a single Gaussian (blue) and double Gaussian (red) fit to the  $\text{H}\alpha$  emission line.

in the simulation is  $7.9 \times 10^{10} \text{ M}_\odot$  meaning that value calculated from observations is in fact an overestimate by factor of  $\sim 1.28$ . As the estimated value is within  $\pm 50$  per cent of the actual value we argue that this is an excellent match and therefore that the total dynamical mass of a G1-like galaxy can be recoverable from observations with HSIM when combined with  $^3\text{D}\text{BAROLO}$  (or a *similar*) during analysis.

It is worth noting that both values of  $v_\theta$  calculated from the two methods used we have employed on the post-HSIM data cubes only differ by  $\sim 1.5 \text{ km s}^{-1}$ , which is an order of magnitude smaller than the error on the measured value of  $v_\theta$ . This would seem to indicate that either method will be reasonably reliable for actual HARMONI observations.

### 4.3 $v_\theta/\sigma$

The dynamical ratio ( $v_\theta/\sigma$ ) has been used to characterize the dynamical state of observed galaxies for over 40 yr (Binney 1978). Galaxies that are isolated and rotationally supported against gravity have larger values of  $v_\theta/\sigma$  (i.e.  $> 1$ , Johnson et al. 2018), while those with smaller values are assumed to be unstable. Pereira–Santaella et al. (2019, henceforth PS19) adds further granularity by assuming those with  $v_\theta/\sigma < 3.2$  are undergoing mergers.

#### 4.3.1 Measurements on galaxy scales

Traditionally this calculation is carried out by calculating a value of  $\sigma$  for the entire galaxy (normally from FWHM of an emission line of the galaxies integrated spectrum), while  $v_\theta$  is taken from the flattest region of the rotation curve. By taking mass weighted mean of the galaxies intrinsic  $\sigma$  values, we are able to calculate  $v_\theta/\sigma$  for G1 as  $340 \text{ km s}^{-1}/150 \text{ km s}^{-1} \sim 2.3$ . Likewise using our arctan fit to the  $^3\text{D}\text{BAROLO}$  model and the fitting a Gaussian profile to the observed  $\text{H}\alpha$  emission line we find a value of  $366.9 \text{ km s}^{-1}/114.2 \text{ km s}^{-1} \sim 3.2$  post-HSIM. The emission line for G1 is actually better fit by a double Gaussian than a simple Gaussian profile (see Fig. 14). This double Gaussian profile arises as a result of the receding side of the galaxy being distinguishable from the approaching side due to the spatial resolution of HARMONI. Calculating  $v_\theta/\sigma$  for the broader Gaussian given  $366.9 \text{ km s}^{-1}/68.8 \text{ km s}^{-1} \sim 5.3$ , while the slimmer gives  $366.9 \text{ km s}^{-1}/61.9 \text{ km s}^{-1} \sim 5.9$ . All four of these  $v_\theta/\sigma$  suggest a gravitationally stable galaxy. If we adopt the PS19 criteria the first two calculated values would suggest that the galaxy is undergoing a merger while the last two suggest the opposite.

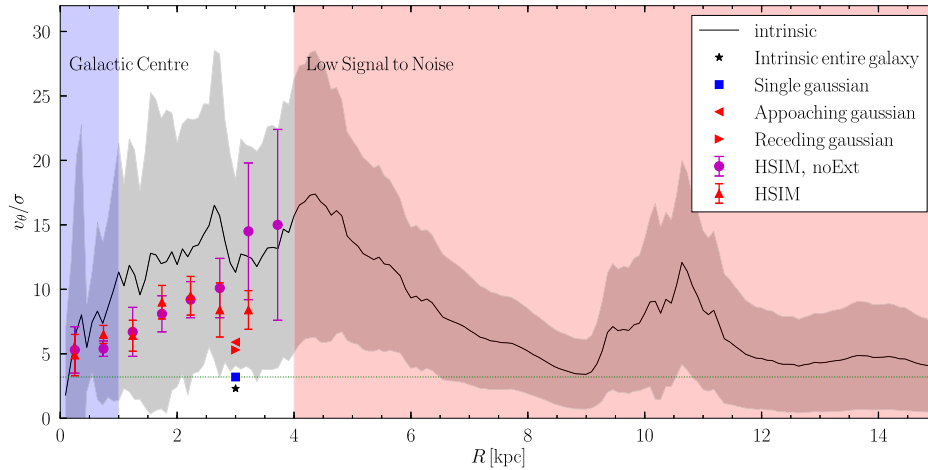


**Figure 15.** Radial profile of  $v_\theta/\sigma$ . The black line shows the intrinsic profile, with the coloured points showing values calculated using  $3^{\text{D}}$ BAROLO after G1 is observed by HSIM. Red points show observations of SSCs that include extinction, while purple show those without extinction. The four data points with no error bars show the value of  $v_\theta/\sigma$  calculated on galaxy-wide scales (see Section 4.3.1 for details). Those points do not depend on  $R$  and are placed at  $R = 3$  kpc by choice. The dotted green line shows  $v_\theta/\sigma = 3.2$ , i.e. the criteria for a merger. The grey-shaded region shows the  $1\sigma$  error on the intrinsic values. The blue shaded region indicates the G1’s galactic centre, while shaded red region shows values of  $R$  where the SNR is too low for  $3^{\text{D}}$ BAROLO to fit observations.

Galaxies at high- $z$  are expected to be more turbulent due to a higher molecular gas fraction (Tacconi, Genzel & Sternberg 2020). The  $v_\theta/\sigma$  ratio for such galaxies would thus be lower and might be interpreted as a galaxy undergoing a merger when in fact it is still finding its equilibrium. To filter this effect, a redshift dependent, threshold velocity dispersion ( $\sigma_0$ ) can be applied (see PS19 and Übler et al. 2019 for a more complete discussion). PS19 advocates that to classify a galaxy as isolated and stable requires  $\sigma < \sigma_0$  and  $v_\theta/\sigma > 3.2$ . Different previous works have defined value of  $\sigma_0$  in different ways. In this work, we use equation 2 of Übler et al. (2019) (as present in equation 5 of H21) to calculate the ‘typical’ value of  $\sigma$  at  $z = 2.2$  as our threshold. Thus, we calculate  $\sigma_0 = 42.9 \pm 6.0$  at  $z = 2.2$ . Combining the  $\sigma_0$  and  $v_\theta/\sigma$  criteria to the observed value and it is not clear whether G1 would be classed as undergoing a merger if measured on a galaxy wide scale due to both a high  $v_\theta/\sigma$  and  $\sigma > \sigma_0$ . If the double Gaussian is resolved and used, either side would suggest a stable/isolated galaxy. These results demonstrate that measuring  $v_\theta/\sigma$  on galaxy wide scales does not provide a clear cut indicator of a settled disc or merger galaxy as normally thought. We discuss the interpretation of  $v_\theta/\sigma$  further in Section 5.3.

#### 4.3.2 Measurements on sub-kiloparsec scales

As outlined above (see Section 2.2.2), it is possible to calculate  $\sigma_{\text{sim}}$  for each cell in the simulation which in turn allows for maps and radial profiles of  $\sigma_{\text{sim}}$  to be calculated (see Figs 8 and 5, respectively). We use the intrinsic radial profiles of  $v_\theta$  and  $\sigma_{\text{sim}}$  to calculate the intrinsic radial profile of  $v_\theta/\sigma$ , which is presented in Fig. 15. From visual inspections of G1, we know that the galaxy is a disc with spiral arms (see Fig. 2) and therefore would expect  $v_\theta/\sigma > 1$ , which we find at all radii. With the exception of  $R < 0.5$  kpc, we find  $v_\theta/\sigma > 5$  for G1. As noted previously (see Section 3), the centre of the galaxy tends to have high values of  $\sigma_{\text{sim}}$  and hence a reduced  $v_\theta/\sigma$ . At larger radii, particularly those capturing the connective gas between G1 and G2,  $v_\theta/\sigma$  decreases however even here the lowest  $v_\theta/\sigma$  reaches is 3.4, which according to the classifications in PS19 would be interpreted as an isolated galaxy. It is worth noting that  $v_\theta/\sigma$  increases within G2,

indicating that the orbiting velocity of G2 about G1 dominates over the signal of any internal  $\sigma$  or  $v_\theta$  of G2. Taking the mean of all  $v_\theta/\sigma$  values within G1 gives  $\langle v_\theta/\sigma \rangle = 12.3 \pm 9.1$ , again confirming the classification of rotationally supported disc. It is worth noting that  $\langle v_\theta/\sigma \rangle$  does not match the value of  $v_\theta/\sigma$  calculated in Section 4.3.1, the implications of this discrepancy are discussed in Section 5.3.

Unlike our simple kinematic model (see Section 4.2.2),  $3^{\text{D}}$ BAROLO calculates a  $\sigma$  value for each ring that it calculates  $v_\theta$  for. The  $\sigma$  radial profile determined by  $3^{\text{D}}$ BAROLO is a good match to intrinsic profile, with high  $\sigma$  near the galactic centre and smaller values at larger radii (see lower panel of Fig. 13). Using the analysis from  $3^{\text{D}}$ BAROLO we are able to calculate the observed radial profile of  $v_\theta/\sigma$  (red data points on Fig. 15). While there are differences between the intrinsic and observed radial profile of  $v_\theta/\sigma$  in general they are in good agreement. For example, within the central kiloparsec  $v_\theta/\sigma$  hovers around 5 while for  $1 < R < 3.5$  kpc  $v_\theta/\sigma$  sits between 5 and 10. As before, due to the SNR cut and low SNR values at  $R > 3.5$   $3^{\text{D}}$ BAROLO is unable to provide any information of  $v_\theta/\sigma$  at large radii. For  $1 < R < 4$  kpc, we find  $\langle v_\theta/\sigma \rangle = 7.6 \pm 1.4$  ( $\langle v_\theta/\sigma \rangle = 9.3 \pm 2.8$  when extinction is neglected). As with the intrinsic measurement this value of  $\langle v_\theta/\sigma \rangle$  would normally be interpreted as G1 being a rotationally supported disc galaxy. For G1 the intrinsic velocity dispersion is less than  $\sigma_0$  with the exception of  $R < 1$  kpc (i.e. galactic centre) and  $R > 8$  kpc (i.e. outside of G1), where we find values as large as  $\sim 123 \text{ km s}^{-1}$  (see the lower panel of Fig. 13). Similarly, we find that the values of  $\sigma$  determined by  $3^{\text{D}}$ BAROLO are very close to  $\sigma_0$  for  $R > 1.5$ . From both of the above two quantitative metrics G1 would be classified as an isolated, rotationally supported, stable galaxy. Yet G1 is known to be at the second periaapsis of a merger with G2 (see Fig. 4) at the time of our analysis. The lack of a merger signature in  $v_\theta/\sigma$  and  $\sigma$  could simply be a result G2 being significantly smaller (only 12.5 per cent of the gas mass) than G1 or the impact parameter of the merger. However, the simplest explanation is that G2 is still too far away from G1 at the time of analysis.  $\sigma$  and hence  $v_\theta/\sigma$  may only show merger signatures once the G2 crosses through the gas or stellar discs. In Grisdale et al. (in preparation), we explore this signature and impact of mergers on G1.

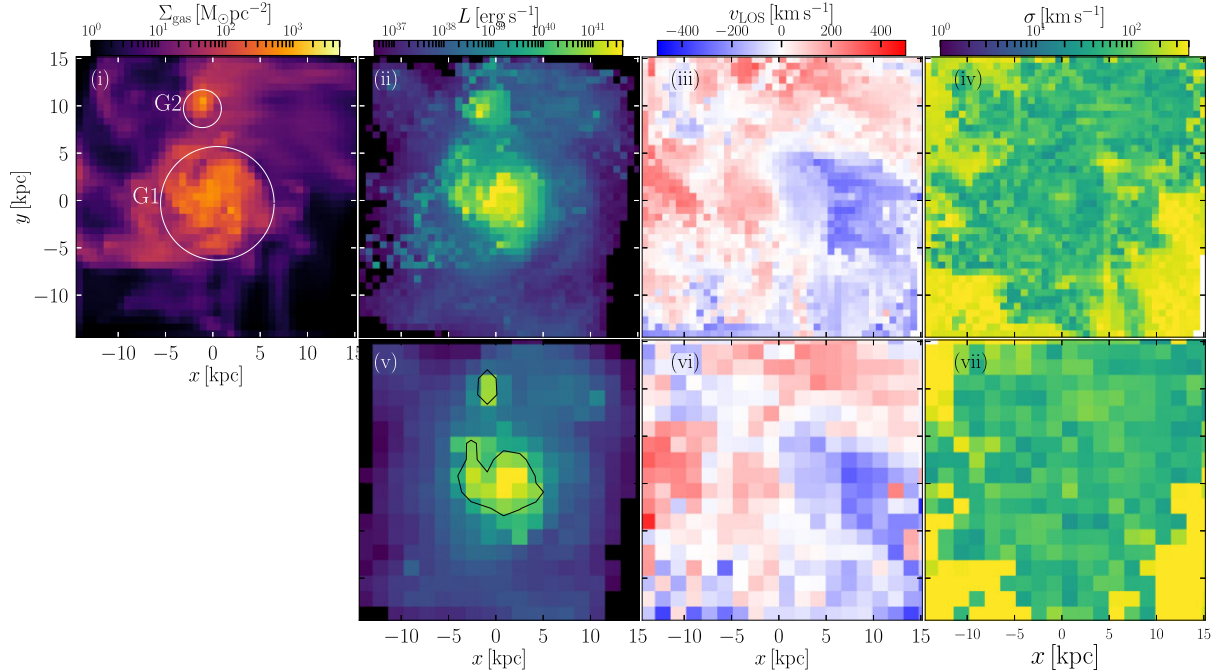


**Figure 16.** Impact of resolution on intensity maps. Top row: Maps of G1 with a spatial resolution of  $\Delta x = 722$  pc. Panel (i) shows the gas surface density map. The white circles are identical to the circles in Fig. 2. Panels (ii), (iii), and (iv) show the corresponding H $\alpha$  zeroth, first, and second moment maps once G1 is processed by LCARS. Bottom row: Mock KMOS observations of the fiducial LCARS data cube (see the text for details). Panels (v), (vi), and (vii) show the H $\alpha$  zeroth, first, and second moment maps, respectively. The contour shown on (v) represents the pixels likely to be detected after applying a SNR cut.

## 5 DISCUSSION

### 5.1 Impact of resolution

#### 5.1.1 Resolution of LCARS

All the results in the previous sections have been calculated using a fixed spatial resolution of  $\Delta x \sim 90$  pc for data cube passed to LCARS and then HSIM. To test the impact of the choice of spatial resolution, we rerun LCARS on G1 with a spatial resolution 8 times lower, i.e.  $\Delta x = 722$  pc. In Fig. 16, we present the pre-LCARS surface density map, as well as the H $\alpha$  zeroth, first, and second moment maps post-LCARS. At  $z = 2.2$ , this corresponds to an angular pixel size of  $\sim 86$  mas which is larger than the biggest pixel size available in HSIM (60 mas), for this reason we do not pass these data cubes through HSIM, instead we carry out our analysis on the LCARS SSC. At this lower resolution the G1 and G2 are still distinguishable in both the surface density map and the post-LCARS H $\alpha$  map. However, in both cases G2 has lost the definition of its internal structure. Some internal structure is visible in G1 however without prior knowledge of it would be next to impossible to determine what form that structure takes.

By comparing the single aperture spectrum of the  $\Delta x = 722$  pc run to fiducial run, we see that the dual Gaussian profile remains (see the top panel of Fig. 17) though the receding peak is reduced and the approaching peak is enhanced. Changing the resolution of LCARS does not change the number of star particles in the simulation but does reduce the number of SSPs and increases the number of stars that contribute to each SSP. Therefore, the same number of photons are concentrated into a smaller number of cells, particularly closer to the galactic centre. This results in the more concentrated luminosity seen in Fig. 17.

Turning to the kinematics, there is again a significant reduction in structures of both the first and second moment maps. With that

being said, comparing panels (iii) and (iv) of Fig. 16 with panels (ii) and (iv) of Fig. 8 shows a general agreement with the kinematic maps created at the fiducial resolution. By applying the same slit-based approach (see Section 4.1.3) to the first moment map of the  $\Delta x = 722$  pc run, we are able to produce a rotation curve for this LCARS run (see the lower panel of Fig. 17). From which we estimate  $v_\theta \sim 467 \text{ km s}^{-1}$ , which would equate to a total mass of  $10^{11.48} M_\odot$  or  $\sim 2.4 \times$  the actual total mass of G1. Allowing  $x_\theta$  to be a fitted parameter we see that reducing the resolution moves  $x_\theta$  to  $\sim -310$  pc which is  $\sim 785$  pc from the true value. When  $x_\theta$  is fitted for in the fiducial resolution run we found  $x_\theta \sim -22$  pc. In either case, the difference is of the order of a single cell and reasonably close to the actual galactic centre.

#### 5.1.2 Resolution of observations: KMOS versus HARMONI

In reality, it will be the distance to a galaxy, as well as the sensitivity and resolution power of the instrumentation used to observe it that will determine the resolution of a data cube used for analysis. Testing this can be achieved by taking the output SSCs from LCARS, reducing the spatial resolution and spectral resolution as well as applying a point spread function (PSF). For comparisons with H21, we opt to reduce the spatial and spectral resolutions to 0.19 arcsec (1.62 kpc) and  $2.8 \text{ \AA}$ , respectively. Additionally, we apply a Gaussian PSF with a FWHM of 0.6 arcsec to mimic values of H21's observations with the KMOS on the VLT.<sup>11</sup> As one might expect, this mock KMOS observation, presented in panel (v) of Fig. 16, shows a significantly degraded H $\alpha$  zeroth moment map. The sites of star formation can no longer be seen and all traces of spiral arms have been lost. Calculating

<sup>11</sup>This is very simple model for a mock observation and should only be used as guide on how observations with HARMONI will differ to those on KMOS.



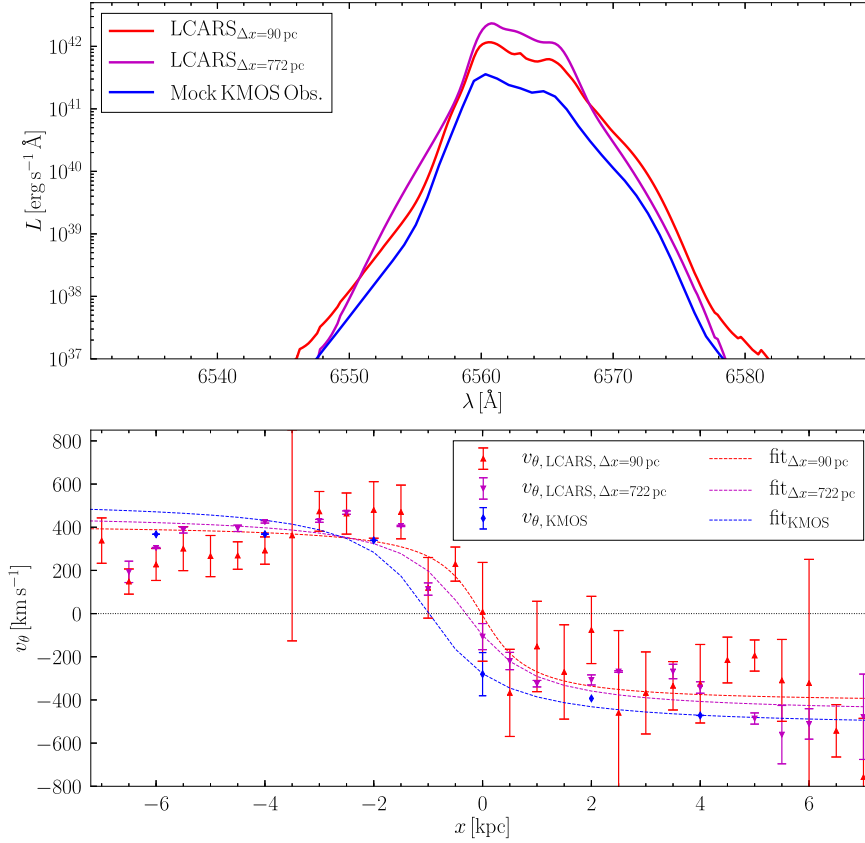


**Figure 17.** Top: Comparison of the impact that different resolutions have on the single aperture (continuum subtracted) spectrum of G1. The red, purple, and blue lines show the fiducial resolution, LCARS run at to  $\Delta x = 772$  pc, and a mock KMOS observation of the fiducial LCARS outputs, respectively. Bottom: Comparison of the rotational velocities when calculated from a slit for the three different resolutions. Dashed lines show arctan fits to the corresponding data points.

a single spectrum from the mock KMOS observations produces a similar, double Gaussian  $H\alpha$  emission line (see the top panel of Fig. 17). Due to the much broader PSF of the mock observation, some photons from the emission line have become indistinguishable from the continuum, which results in the luminosity of the emission being reduced to  $\sim 0.3$  of full resolution LCARS  $H\alpha$  emission line. This effect is normally accounted for using a point source with a known luminosity to calibrate the observations.

Panels (vi) and (vii) of Fig. 16 shows the first and second moment maps for these mock observations. At the resolution of these mock observations, the kinematic structure of the galaxy is, again, severely degraded. We again apply a slit across the first moment map and calculate a rotation curve (shown in the lower panel of Fig. 17). This calculation estimates  $v_\theta = 533 \text{ km s}^{-1}$  and  $x_\theta = -513$  pc. This places the calculated centre of rotation almost a kiloparsec from the intrinsic centre of rotation, and overestimates the G1’s rotation speed by a factor of  $\sim 1.6 \times$  faster than its true value. Given the very low spatial resolution and the wide PSF, this significant overestimate is understandable and highlights the importance of being able to resolve a galaxy sufficiently that kinematic measurements are representative of the observed galaxy.

Until this point, we have assumed that mock KMOS observations have an  $\text{SNR} > 3$  for all spaxels. Realistically, this is not the case and low SNR spaxels should be accounted for in our mock observations. To this end, we assume that the highest signal-to-noise ratio found is 20 and that this is found in the most luminous pixel of the zeroth

moment map. We mask all pixels that fall below one twentieth of the luminosity of that pixel [pixel above this cut are shown via the contour in panel (v) of Fig. 16]. With this SNR cut in place G1 loses further structural definition and G2 is reduced to a single pixel. The measured SFR of the galaxy is negligibly affected by the SNR cut. There is an insufficient number of pixels remaining in the first moment map to calculate a trustable  $v_\theta$  value and for this reason we do not attempt to. In short, once the prospect of noise is accounted for it is no longer possible to recover, let alone realistic, kinematics from our mock KMOS observations.

We assert that a physical comparison between panel (iii) of Fig. 10 and panel (v) of Fig. 16 presents a strong argument for the need for high spatial and spectral resolution offered by the 30 m-class telescope. Furthermore, without relying on a proxy, such as  $v_\theta/\sigma$ , detection of minor mergers is extremely difficult, as is the detection of inflows and outflows. As discussed in Section 5.3, even  $v_\theta/\sigma$  has issues associated with it when calculated on large scales, and so should be used with caution. Simply put observations on the ELT in general and with HARMONI specifically have the potential to be game changing in the exploration of galaxies at high redshifts ( $z \gtrsim 2$ ).

It is worth noting that the ELT will allow galaxies at a range of redshifts to be probed on scales of  $\sim 100$  pc. If these new observations of high-redshift galaxies have clumpy structures, similar to simulated galaxy in this work, new analysis tools will likely be required. We will be exploring this in upcoming work.

## 5.2 Are H $\alpha$ photons a good tracers for gas kinematic properties?

This work focuses on exploring whether the intrinsic properties of a galaxy can be recovered from observations, such as those taken with HARMONI on the ELT. Our results show that in general this is the case; however, there are noticeable differences between intrinsic and observed properties. For example, as noted in Section 4.1.3 and seen in Fig. 8, the map  $v_{\text{LOS, obs}}$  has several pockets of gas moving at speeds on the order of  $500 \text{ km s}^{-1}$  which are not present in the map of  $\langle v_{\text{LOS}} \rangle$ . To properly understand how the observations link back to intrinsic properties of a galaxy, it is necessary to understand where these high velocity regions come from.

The answer to this question is weighting. In the case of the intrinsic map each pixel in the map is a mass weighted average of all cells along the line of sight, while in the  $v_{\text{LOS, obs}}$  map each pixel is the result from the photons summed along the line of sight. When mass weighting, the spiral arms dominate the rotation signature at a given  $R$ . However, in the latter case photons are removed due to extinction in the arms. Photons that have to travel through dense gas, such as the spiral arms, have their contribution to  $v_{\text{LOS, obs}}$  reduced. Areas of the galaxy with low-density gas (e.g. inter-arm gas) are affected to a lesser degree and so their contributions are effectively boosted.

We see an example of this is the region found at  $(-3.0, 0.5)$  on panel (i) of Fig. 2 that corresponds to the  $v_{\text{LOS, obs}} \sim 500 \text{ km s}^{-1}$  region found at the same location in panel (ii) of Fig. 8. This region is located behind a spiral arm and ahead of two large gas clouds as a result has very little extinction meaning that the brightest cells in this region will dominate the measurement of  $v_{\text{LOS, obs}}$ . From panels (ii) and (iii) of Fig. 2, we know there are only ‘old’ stars in this region, i.e. all with ages greater than 10 Myr. Such stars are unlikely to provide a sufficient injection of energy to drive gas to such velocities. Instead, we have to look to the surrounding gas, which does have young stars. Panel (iii) of Fig. 8 shows this region to have mass weighted  $\sigma$  in excess of  $30 \text{ km s}^{-1}$ , while panel (iv) shows values of  $> 200 \text{ km s}^{-1}$ . Combining all the available information we are able to determine the source of such high-velocity regions seen only in the photon ‘weighted’ maps. The galactic disc contains regions of low-density, inter-arm gas. This is being heated by young stars in the surrounding arms and gas clumps, which accelerate the gas to speeds of several hundred kilometres a second. The old stars plus diffuse photons from the neighbouring young stars (see Section 2.2.4) illuminate the region sufficiently for the high  $v_{\text{LOS, obs}}$  to be seen in panel (ii) of Fig. 8. However, when mass weighting to create the  $\langle v_{\text{LOS}} \rangle$  map the gas ‘above’ and ‘below’ the galaxy contribute to  $\langle v_{\text{LOS}} \rangle$  and bring the mean value down. By taking a slice through G1 at the correct depth, it is possible to create  $v_{\text{LOS}}$  map that will show the high-velocity region seen at  $(-3.0, 0.5)$ . By creating slices at multiple depths, it would be possible map all the high-velocity pocket within G1.

This effect is still present after the SSC has been passed through HSIM and is at least partially responsible for the larger value of  $v_\theta$  found at  $R = 2.25 \text{ kpc}$ . Indeed, by looking at (ii) of Fig. 11 there are small regions or ‘bubbles’ of high  $v_{\text{LOS, obs}}$  on the approaching side of the galaxy. Weighting one side of the galaxy preferentially over the other when carrying out analysis can reduce  $v_\theta$  in several places, by ignoring such regions. It’s also worth noting that we found that stellar feedback-driven outflows and corresponding inflows (as gas falls back on to the galaxy) could impact the values of  $v_\theta$  and  $\sigma$  determined by <sup>3D</sup>BAROLO. Again these are low-density, high-velocity structures and thus have low mass but strong-photon weighting. This result highlights how a small-scale structures within the

galaxy can impact the measured physical properties recovered from observations.

Despite the discussion above, it is clear that the spiral arms and galactic centre still provide the majority of the H  $\alpha$  emissions in our HSIM observations (see Figs 6 and 10). Furthermore, as we showed throughout Section 4, it is possible to recover reasonable measurements of G1’s SFR, rotation curve, and dynamical ratio profile. In summary, there is limited fungibility between mass and photon weighting when determining the properties of a galaxy however it is possible to use the latter to get good estimates of a galaxies intrinsic properties. In the case of all real galaxies in the physical Universe, it is highly unlikely we will be able to directly measure their properties as we can in simulations, therefore it is highly important to know the limits of how observations can be translated back to the galaxy’s physical properties.

## 5.3 Importance of $v_\theta/\sigma$

Section 4.3 showed various ways of calculating the dynamical ratio,  $v_\theta/\sigma$ , with each method resulting in different calculated values. All of the methods used to calculate  $v_\theta/\sigma$  in this work have found G1 to be a rotationally supported disc; however, the method used can change the measured value by as much as a factor of  $\sim 6$ . If this ratio is to be used as a measure of a galaxies gravitational stability, or an indicator of a merger, this presents a problem: which method should be considered, which is valid and when is it valid? We discuss those difficulties here.

The first method looked at the global properties of a galaxy (e.g. width of single aperture spectrum and the flattest part of the rotation curve, see Section 4.3.1), in this work  $v_\theta/\sigma$  was calculated on scales of 12 kpc (i.e. the diameter of G1). This kind of approach makes sense when the internal structure of a galaxy cannot be resolved, such as when current generation of 10 m-class telescope carry out observations of galaxies at  $z \sim 2$ , e.g. see our mock KMOS observations above or Fig. 2 of H21. Due to the  $\sim 4.75 \times$  larger increase in the primary mirror diameter combined with the adaptive optics of ELT, we see a  $\sim 9.8 \times$  increase in spatial resolution at  $z \sim 2.2$  with the ELT over the VLT. This allows for structures such as spiral arms to be resolved within the galaxy as well as being able to resolve the velocity dispersion on sub-kiloparsec scales and thus radial profiles of  $v_\theta$ ,  $\sigma$  &  $v_\theta/\sigma$  to be calculated.

In Section 5.2, we discussed the impact of using photon weighting rather than using mass weighting when calculating properties of galaxies. Here, we see another example of the impact the type of weighting has. When taking the single aperture spectrum of a galaxy the brightest regions will dominate the spectrum, furthermore bright regions with low  $\sigma$  will contribute more to the shape of the emission line than equally bright (i.e. the integral of the emission line is the same), high  $\sigma$  regions as the latter can become lost in the continuum. These complications need to be considered when using a single aperture spectrum to determine  $\sigma$  and  $v_\theta/\sigma$ .

We have already seen that the expected spatial resolution of observations with HARMONI should allow for  $\sigma$  to be resolved on sub-kiloparsec scales and thus for a determination of how  $v_\theta/\sigma$  changes within a galaxy (e.g. see Fig. 15) becomes possible. As a result we need to (re)evaluate what  $v_\theta/\sigma$  on such scales mean. The intrinsic  $v_\theta/\sigma$  profile is mass weighted as a result will be dominated by the velocity structures of arms (see Section 5.2). Therefore, the  $v_\theta/\sigma$  profile provides a measure of whether internal velocity structures of clouds and spiral arms at a given radius are more important than galactic rotation. For example, if at some radius  $v_\theta/\sigma$  is found to be much greater than 1, it would be a strong indicator that

GMCs or spiral arms have relatively little internal turbulence and are simply clumps of gas moving around within the galaxy. However if  $v_\theta/\sigma \leq 1$  for a given  $R$ , this would suggest that the GMCs are highly turbulent, to such a degree that their internal motions are comparable to the speed at which the cloud is orbiting the galaxy. Finally, if  $v_\theta/\sigma < 1$  is found at a given  $R$ , this would be a strong indicator that gas structures are either rapidly collapsing due to gravity or being blow apart (most likely by stellar feedback).

Such interpretations are complicated when inferred from observations, where brightest regions *may* not be tracing mass. That being said, given our discussion in Section 5.2 it is clear that the H $\alpha$  emission lines in our mock observations at least partially trace the gas mass. In which case the above interpretation of a galaxies radial  $v_\theta/\sigma$  profile should hold.

Calculating the mean dynamical ratio for the galaxy from the radial profiles ( $\langle v_\theta/\sigma \rangle$ ) also proved to be different to galaxy-scale calculation. The brightest part of G1 is the galaxy's centre (see Fig. 10), as a result this region has a significant impact on the shape of the H $\alpha$  emission line for galaxy. Especially given that the highest values of  $\sigma$  are found at  $R < 1$ , i.e. the galactic centre. Furthermore, while  $v_\theta$  tends to be higher in this region, it is only by a factor of  $\sim 1.2$ , compared with  $\sigma$  increasing by a factor of  $\gtrsim 2.5$  and thus  $v_\theta/\sigma$  in the galactic centre is lower. In essence the traditional observer's method of measuring a single value of  $\sigma$  and  $v_\theta$  for the galaxy is biased towards the galaxies centre where  $\sigma$  is higher, while  $\langle v_\theta/\sigma \rangle$  gives a measurement that accounts for the entire galaxy. With the above in mind, we would not expect to see signature of a minor merger in single spectrum calculated  $v_\theta/\sigma$  until either 1) the two galaxies are close enough to disrupt the galactic centre of the primary galaxy or 2) there is sufficient star formation occurring, in the gas connecting the two galaxies, that the galactic centre no longer dominates the single-aperture spectrum.

Finally, we highlight that all of our calculations of  $v_\theta/\sigma$  are carried out at specific scales, e.g. galaxy wide, 500 pc rings, etc. As shown in Agertz, Romeo & Grisdale (2015), the scale used when measuring any stability criteria will impact the apparent stability of a galaxy. We therefore remind the reader that with any criteria used to determine stability, even a simple one such as  $v_\theta/\sigma$  it is important to consider which scales the calculation is carried out on.

## 6 CONCLUSION

In this work, we explored whether it is possible to accurately recover the intrinsic properties of a galaxy at a redshift of  $z \sim 2.2$  with the ELT and the HARMONI spectrograph. To achieve this, we passed a galaxy, from the cosmological simulations NEWHORIZON, through the post-processing pipeline LCARS (v2.0) to add photons to the simulations. The resulting H $\alpha$  SSC was then observed using the HARMONI simulator (HSIM) and analysed. The galaxy used in this work, which we label G1, is the primary galaxy in a merging pair. At the time of this analysis, the secondary galaxy, G2, is at the periapsis of its second orbit of G1. Our key results are as follows:

(i) After being processed with LCARS and observed with HSIM the morphology of the G1 remains visible: spiral arms are clearly seen, as is a bright galactic centre and the more diffuse gaseous disc. Post-HSIM the morphology more closely resembles a map of the young (ages  $< 10$  Myr) stars within the galaxy.

(ii) Measuring the SFR before and after observation recovers values that are larger than the intrinsic SFR of the galaxy ( $38.3 \text{ M}_\odot \text{ yr}^{-1}$ ). In the case of the former, we recover a value of  $65.8 \text{ M}_\odot \text{ yr}^{-1}$  when correcting for extinction and  $59.1 \text{ M}_\odot \text{ yr}^{-1}$  if extinction is not

added by LCARS. For the latter, we find  $\text{SFR} = 69.3 \text{ M}_\odot \text{ yr}^{-1}$  when correcting for extinction. Both sets of values are within a factor of 2 of the intrinsic value.

(iii) First moments maps of G1 show that the line-of-sight velocity structure of G1 is largely recoverable from the H $\alpha$  emission line. After observation, there is a reduction in the detail of the first moments map; however, the key features remain. The second moment map of G1's SSC shows larger regions of high velocity dispersion ( $\sigma$ ) than the intrinsic map. These high  $\sigma$  are reduced in the observed second moment map due to originating in the inter-arm, low-density, non-star-forming gas, i.e. regions with low SNR.

(iv) Applying a slit to the first moments map, perpendicular to the axis of inclination, allow for G1's rotation curve to be recovered with good accuracy from the SSCs. After being observed too much internal structure is lost for a slit to be effective. An analysis tool, such as <sup>3D</sup>BAROLO, is able to produce a rotation curve that reasonably matches the intrinsic curve of the galaxy. From these curves, an estimate of the G1's mass is recoverable and found to be within  $\pm 40$  per cent of the intrinsic total mass.

(v) We calculate the dynamical ratio ( $v_\theta/\sigma$ ) in several ways. In all cases finding G1 to be considered rotationally support against gravity (i.e.  $v_\theta/\sigma > 1$ ). Calculating  $v_\theta/\sigma$  on a galaxy wide scale (using the peak of the rotational curve and width of a single aperture spectrum) finds a value of 2.3 intrinsically and 3.2 after observation. However, both of these values are dominated by the galaxies centre and are not representative of the entire galaxy. Calculating  $v_\theta/\sigma$  as a function of radius using the galaxies rotation curve and radial  $\sigma$  profile shows that the majority of the galaxy has  $v_\theta/\sigma > 10$  ( $> 5$  from HSIM observations). Furthermore, averaging the  $v_\theta/\sigma$  profile provides a very different global picture of the galaxy the compared with  $v_\theta/\sigma$  calculated on a galaxy wide scale, e.g. 7.6 versus 3.2, as the former uses data from throughout the galaxy while the latter is dominated to the galactic centre. We also note that the galactic-scale calculation can be influenced by the interpretation of the emission line, e.g. is it a single or double Gaussian profile and thus what is its width.

While we have shown that the physical/intrinsic properties of a galaxy can be recovered to a reasonable degree from photons emitted by that galaxy, we have also shown that emissions can be impacted by low density gas and thus do not provide an accurate representation of the properties of the majority of the gas along a line of sight. In short, measuring properties via emission lines is not a replacement for being able to measure the gas properties directly. However, given that the latter is likely impossible the former will have to be sufficient.

In conclusion, by using a HARMONI on the ELT it will be possible to calculate the physical properties of a galaxy at  $z \sim 2.2$ , including its SFR, kinematic structure, rotation curve, total mass, and  $v_\theta/\sigma$  profile. However, we advise careful consideration of methods as how low SNR regions are handled can impact the SFR measurement, while choice of scale can lead to drastically different interpretations of how much a galaxy is rotationally supported. Finally, we emphasize that the primary goal of this work is to determine if the galaxy's intrinsic properties are recoverable. To that end the settings used for the HSIM observations and analysis are tuned to provide the best possible result.

## ACKNOWLEDGEMENTS

We thank the referee for the useful and constructive comments. KG and NT acknowledge support from the Science and Technology Facilities Council (grants ST/N002717/1 and ST/S001409/1), as



part of the UK E-ELT Programme at the University of Oxford. KG, LH, DR, JD, AS, and IGB acknowledge support from STFC through grant ST/S000488/1. The research of JD and AS is supported by Adrian Beecroft and STFC. MPS acknowledges support from the Comunidad de Madrid through Atracción de Talento Investigador Grant 2018-T1/TIC-11035 and PID2019-105423GA-I00 (MCIU/AEI/FEDER,UE). SKY acknowledges support from the Korean National Research Foundation (NRF-2020R1A2C3003769). KK acknowledges support from the DEEPDIP project (ANR-19-CE31-0023). This project has received funding from the European Research Council (ERC) under the European Union's Horizon 2020 research and innovation programme (grant agreement no. 693024). This work was granted access to the HPC resources of CINES under the allocations c2016047637, A0020407637 and A0070402192 by Genci, KSC-2017-G2-0003 by KISTI, and as a 'Grand Challenge' project granted by GENCI on the AMD Rome extension of the Joliot Curie supercomputer at TGCC. The supercomputing time for numerical simulation was kindly provided by KISTI (KSC-2017-G2-0003), and large data transfer was supported by KREONET, which is managed and operated by KISTI. Calculations were performed with version 17.01 of CLOUDY (Ferland et al. 2017) and HSIM version 3.03 (see <https://github.com/HARMONI-ELT/HSIM>). We thank JWB for fruitful discussions.

## DATA AVAILABILITY

The data underlying this article will be shared on reasonable request to the corresponding author.

## REFERENCES

- Agertz O., Romeo A. B., Grisdale K., 2015, *MNRAS*, 449, 2156
- Arribas S., Colina L., Monreal-Ibero A., Alfonso J., García-Marín M., Alonso-Herrero A., 2008, *A&A*, 479, 687 [https://ui.adsabs.harvard.edu/link\\_gateway/2008A&A...479..687A/doi:10.1051/0004-6361:20078451](https://ui.adsabs.harvard.edu/link_gateway/2008A&A...479..687A/doi:10.1051/0004-6361:20078451)
- Binney J., 1978, *MNRAS*, 183, 501
- Bondi H., Hoyle F., 1944, *MNRAS*, 104, 273
- Chabrier G., 2005, *ASSL*, 327, 41
- Cirasuolo M. et al., 2020, *Proc. SPIE*, 11447, 6
- Daddi E. et al., 2007, *ApJ*, 670, 156 [https://ui.adsabs.harvard.edu/link\\_gateway/2007ApJ...670..156D/doi:10.1086/521818](https://ui.adsabs.harvard.edu/link_gateway/2007ApJ...670..156D/doi:10.1086/521818)
- Domínguez A. et al., 2013, *ApJ*, 763, 10
- Dubois Y., Devriendt J., Slyz A., Teyssier R., 2012, *MNRAS*, 420, 2662
- Dubois Y. et al., 2014, *MNRAS*, 444, 1453
- Dubois Y. et al., 2021, *A&A*, 651, 29
- Elbaz D. et al., 2011, *A&A*, 533, 26
- Epinat B., Contini T., Le Fèvre O., Vergani D., Garilli B., Amram P., Queyrel J., Tasca L., Tresse L., 2009, *A&A*, 504, 789
- Ferland G. J. et al., 2017, *Rev. Mex. Astron. Astrofis.*, 53, 385
- Fitzpatrick E., 1999, *PASP*, 111, 63
- Grisdale K., 2021, *MNRAS*, 500, 3552
- Grisdale K., Agertz O., Romeo A. B., Renaud F., Read J. I., 2017, *MNRAS*, 466, 1093
- Grisdale K., Thatte N., Devriendt J., Pereira-Santaella M., Slyz A., Kimm T., Dubois Y., Yi S. K., 2021, *MNRAS*, 501, 5517
- Hogan L., Rigopoulou D., Magdis G. E., Pereira-Santaella M., García-Bernete I., Thatte N., Grisdale K., 2021, *MNRAS*, 503, 5329, [https://ui.adsabs.harvard.edu/link\\_gateway/2021MNRAS.tmp...567H/doi:10.1093/mnras/stab527](https://ui.adsabs.harvard.edu/link_gateway/2021MNRAS.tmp...567H/doi:10.1093/mnras/stab527)
- Hoyle F., Lyttleton R. A., 1939, *Proc. Cambridge Phil. Soc.*, 35, 405
- Iliev I. T. et al., 2009, *MNRAS*, 400, 1283
- Johnson H. L. et al., 2018, *MNRAS*, 474, 5076
- Kahre L. et al., 2018, *ApJ*, 855, 16
- Kannan R., Vogelsberger M., Marinacci F., McKinnon R., Pakmor R., Springel V., 2019, *MNRAS*, 485, 117
- Kaviraj S. et al., 2017, *MNRAS*, 467, 4739
- Kennicutt R. C., 1998, *AJ*, 498, 541
- Kennicutt R. C., Tamblyn P., Congdon C. E., 1994, *ApJ*, 435, 22 [https://ui.adsabs.harvard.edu/link\\_gateway/1994ApJ...435...22K/doi:10.1086/174790](https://ui.adsabs.harvard.edu/link_gateway/1994ApJ...435...22K/doi:10.1086/174790)
- Kimm T., Cen R., 2014, *ApJ*, 788, 18
- Kimm T., Katz H., Haehnelt M., Rosdahl J., Devriendt J., Slyz A., 2017, *MNRAS*, 466, 4826
- Leitherer C. et al., 1999, *ApJS*, 123, 3
- Madau P., Dickinson M., 2014, *ARA&A*, 52, 415
- Murphy E. J. et al., 2011, *ApJ*, 737, 16
- Noeske K. G. et al., 2007, *ApJ*, 660, L43
- Osterbrock D. E., 1989, *Astrophysics of Gaseous Nebulae and Active Galactic Nuclei*. University Science Books, Melville, NY, USA
- Park M.-J. et al., 2019, *ApJ*, 883, 17
- Peebles M. S., Werk J. K., Tumlinson J., Oppenheimer B. D., Prochaska J. X., Katz N., Weinberg D. H., 2014, *ApJ*, 786, 17 [https://ui.adsabs.harvard.edu/link\\_gateway/2014ApJ...786...17P/doi:10.1088/0004-637X/786/1/54](https://ui.adsabs.harvard.edu/link_gateway/2014ApJ...786...17P/doi:10.1088/0004-637X/786/1/54)
- Pereira-Santaella M. et al., 2019, *MNRAS*, 486, 5621 [https://ui.adsabs.harvard.edu/link\\_gateway/2019MNRAS.486.5621P/doi:10.1093/mnras/stz1218](https://ui.adsabs.harvard.edu/link_gateway/2019MNRAS.486.5621P/doi:10.1093/mnras/stz1218)
- Puech M., Hammer F., Lehnert M. D., Flores H., 2007, *A&A*, 466, 83=92
- Richardson M. L. A., Routledge L., Thatte N. and Tecza M., Houghton R. C. W. and Pereira-Santaella M., Rigopoulou D., 2020, *MNRAS*, 498, 1891
- Romeo A. B., Burkert A., Agertz O., 2010, *MNRAS*, 407, 1223
- Rosdahl J., Blaizot J., Aubert D., Stranex T., Teyssier R., 2013, *MNRAS*, 436, 2188
- Rosdahl J., Katz H., Blaizot J. and Kimm T., Michel-Dansac L., Garel T., Haehnelt M., Ocvirk P., Teyssier R., 2018, *MNRAS*, 479, 994
- Schmidt M., 1959, *ApJ*, 129, 243
- Schreiber C. et al., 2015, *A&A*, 575, 29
- Speagle J. S., Steinhardt C. L., Capak P. L., Silverman J. D., 2014, *ApJS*, 214, 52
- Stott J. P. et al., 2016, *MNRAS*, 457, 1888
- Strömgren B., 1939, *ApJ*, 89, 526
- Tacconi L. J., Genzel R., Sternberg A., 2020, *ARA&A*, 58, 157
- Tamai R., Cirasuolo M., González J. C., Koehler B., Tuti M., 2016, *Proc. SPIE*, 9906, 13
- Teodoro E. D., Fraternali F., 2015, *MNRAS*, 451, 3021
- Teyssier R., 2002, *A&A*, 385, 337
- Thatte N. A. et al., 2014, *Proc. SPIE*, 9147, 11
- Toomre A., 1964, *ApJ*, 139, 1217
- Walter F., Brinks E., de Blok W., Bigiel F., Kennicutt R. C. Jr., Thornley M., Leroy A., 2008, *AJ*, 136, 2563
- Whitaker K. E. et al., 2014, *ApJ*, 795, 20
- Wisnioski E. et al., 2019, *ApJ*, 886, 25
- Zieleniewski S., Thatte N., Kendrew S., Houghton R. C. W., Swinbank A. M., Tecza M., Clarke F., Fusco T., 2015, *MNRAS*, 453, 3754
- Übler H. et al., 2019, *ApJ*, 880, 24

This paper has been typeset from a  $\text{\LaTeX}$  file prepared by the author.